MODELING AND CONTROL OF MULTI-ROTOR UAVS:

DESIGN FOR SAFETY AND PERFORMANCE

A Thesis

Submitted to the Faculty of Graduate Studies and Research

In Partial Fulfillment of the Requirements

For the Degree of

Master of Applied Science

in

Industrial Systems Engineering

University of Regina

By

Mojtaba Hedayatpour

Regina, Saskatchewan

May 2018

UNIVERSITY OF REGINA

FACULTY OF GRADUATE STUDIES AND RESEARCH

SUPERVISORY AND EXAMINING COMMITTEE

Mojtaba Hedayatpour, candidate for the degree of Master of Applied Science in Industrial Systems Engineering, has presented a thesis titled, ***Modeling and Control of Multi-Rotor UAVS" Design for Safety and Performance,*** in an oral examination held on May 7, 2018. The following committee members have found the thesis acceptable in form and content, and that the candidate demonstrated satisfactory knowledge of the subject material.

External Examiner: *Dr. Mojtaba Ahmadi, Carleton University

Co-Supervisor: *Dr. Mehran Mehrandezh, Industrial Systems Engineering

Co-Supervisor: *Dr. Farrokh Janabi-Sharifi, Adjunct

Committee Member: Dr. Abdul Bais, Industrial Systems Engineering

Committee Member: Dr. Denise Stilling, Industrial Systems Engineering

Chair of Defense: Dr. Irfan Al-Anbagi, Electronic Systems Engineering

*Participated via SKYPE

ABSTRACT

Recently, a class of unmanned aerial vehicles (UAVs) called multi-rotors has gained significant attention. Despite remarkable progress in control and design of multi-rotors in the past decade, two issues, namely endurance and safety, still remain of main concerns. This thesis mainly aims at investigating about modeling and control of multi-rotor UAVs while focusing on safety, performance and optimal design.

A complete model for forces and moments of a propeller in presence of freestream is presented which helps to derive mathematical models for two different types of multi-rotor UAVs: i) quadcopters with angled thrust vector; and ii) spinning multi-rotors with streamline-shape fuselage.

Afterwards, equilibrium states and the constraints for both types of vehicles are introduced and using control design techniques, we develop flight control strategies to control attitude and position of the vehicle. The following control strategies are developed for: i) quadcopters with no rotor failures; ii) quadcopters with one rotor failure; and iii) spinning multi-rotors.

Also, the performance of the proposed multi-rotor UAVs is investigated in three different topics: i) optimality of the hover solutions in terms of power consumption; ii) stability of the vehicle in different configurations; and iii) controller performance

in trajectory tracking. First, this section leads to introducing six different configurations for quadcopters ranking from the most stable to the most maneuverable which are presented analytically for the first time. Second, a specific configuration for a quadcopter is introduced that leads to the minimum power consumption during a yaw-rate-resolved hovering after a rotor failure. Third, we present optimal design for spinning multi-rotors featuring minimum power consumption and best trajectory tracking performance.

Furthermore, a framework for controlled emergency landing of a quadcopter, with a rotor failure and away from sensitive areas, is presented. Given a 3D representation of the environment, an optimal flight path towards a safe crash landing spot, while avoiding obstacles, is developed using RRT* algorithm. The cost function for determining the best landing spot consists of: (i) clearance from the obstacles; and (ii) distance from the landing spot. Finally, the framework is tested via nonlinear simulations and results are presented.

First Advisor: Dr. Mehran Mehrandezh, University of Regina

Second Advisor: Dr. Farrokh Janabi-Sharifi, Ryerson University

ACKNOWLEDGMENTS

TABLE OF CONTENTS

LIST OF TABLES

LIST OF FIGURES

SYMBOLS

$\boldsymbol{\omega}_p$ angular velocity vector of propeller

$\boldsymbol{V}_\infty$ freestream velocity vector

R_b blade radius

r_b distance of the blade element from the root of the blade

dr_b width of the blade element

ψ_p azimuth angle of propeller

c chord of the blade

ρ_a air density

C_L lift coefficient

C_D drag coefficient

f_p propeller thrust force

τ_{d_p} propeller moment due to drag

τ_p propeller moment due asymmetric lift distribution

Θ angle of attack

Θ_{eff} effective angle of attack

σ lift slope

β dihedral angle

α twist angle

$\boldsymbol{\omega}_B$	angular velocity vector of the body of the vehicle
$\mathbf{I}^B$	moment of inertia matrix of the body of the vehicle
$\mathbf{I}^p$	moment of inertia matrix of the propeller
$\dot{\gamma}$	z-component of angular velocity vector of propeller
$\boldsymbol{\tau}_{d_B}$	moment due to drag of the body of the vehicle
$\boldsymbol{g}$	gravitational acceleration
δ	tilting angle of the rotors in spinning UAV
(p, q, r)	roll, pitch and yaw rates of the vehicle
(ϕ, θ, ψ)	Euler angles
m	mass
λ	drag coefficient in yaw motion
ρ	tunning parameter in finding hover solution
ξ	damping ratio
ω_n	natural frequency
u	control input
$k_l qr$	lqr controller gain matrix
k_p	proportional gain
k_d	derivative gain
P	power
M_i	a coordinate frame named M attached to the $i^t h$ propeller
ζ	damping coefficient in rotational motion
$\mathbf{Q}, \mathbf{R}$	LQR controller weight matrices

P_s	specific power
l	distance of COM of the propeller from COM of the vehicle
c_B	chord of the blade for fuselage
c_p	chord of the blade for propeller
R_B	blade radius for fuselage
R_p	blade radius for propeller
f_B	streamline-shape fuselage thrust force

ABBREVIATIONS

AOA   angle of attack

BET   blade element theory

COM   center of mass

e.g.   exempli gratia

Fig   figure

GVD   generalized Voronoi diagram

LQR   linear quadratic regulator

NACA   national advisory committee for aeronautics

PID   proportional-integral-derivative

RRT   rapidly-exploring random trees

THOR   transformable hovering rotorcraft

UAV   unmanned aerial vehicle

w.r.t.   with respect to

1

Introduction

1.1 Literature Review

Multi-rotors have gained significant attention in recent years. Due to their simplicity and maneuverability, they have been used in a broad spectrum of applications such as bio-engineering [1], agronomy [2] , calibrating antenna of a telescope [3], sports [4] and inspection of infrastructures [5].

A special type of multi-rotors with four motors, known as quadcopters, has been extensively studied and there is a vast literature about their modeling, design, control and path planning. These vehicles normally have an even number of propellers half of which turn in the opposite direction of the remaining propellers. Modeling and full control of a quadcopter can be found in [6]. Quadcopters with fixed rotors fall under the under-actuated and non-holonomic flying machine categories. In the past

decades, many different control strategies have been developed to deal with their under-actuation to improve their performance, agility and stability [7], [8].

In modeling of UAVs, aerodynamic model of propellers plays an important role as it determines the majority of forces and moments in the system. Therefore, an accurate model for the propellers is crucial in analyzing such a system. In the literature, typically, the thrust force and moment generated by the propeller is assumed to be proportional to the square of its angular velocity and the effects of freestream on its performance is usually neglected by assuming small freestream velocities [9], [10], [11]. However, this model is not valid in high speed flight and its accuracy deteriorates as flight speed increases [12], [13].

Recently, there have been considerable attempts on designing simpler flying vehicles with the minimum number of actuators. For example, a controllable flying vehicle with only one moving part can be found in [14] and a swashplateless controllable co-axial UAV can be found in [15]. Altogether, these simple flying vehicles can be classified under three different categories: (1) Samara-type vehicles, (2) flapping wing UAVs, and (3) spinning UAVs.

The vehicles in the first category are inspired from nature through unpowered flight in maple/pine seeds (or Samaras) [16]. They offer a passively-stable flight with slow-rate descending altitude, therefore they would require no active control. A small propulsion system has been added to the body, in lab-scale prototypes, to control the rotational speed and correspondingly the descending rate [16].

The vehicles in the second category are inspired from birds. They normally have one or two flapping wings. Single actuator (wing) vehicles of this category are only capable of altitude control, while those with two actuators (i.e., two wings) are capable of controlling all three translational degrees of motion [17].

Flying machines falling into the third category, namely spinners, generate a constant rotation about a fixed axis in space, precession axis, due to the presence of unbalanced moments in the system (aka, boomerang-type spinners). The minimum number of actuators required to achieve position control in these machines is one, which renders itself as the simplest structure of rotary-wing UAV that is controllable in all translational degrees of motion [18].

Technical specifications of a spinner-type machine with only one actuator, (aka, a monospinner) can be found in [14]. Spinners with two, three and four actuators can also be found in [18]. A novel design of a small spinning vehicle that consists of one single propeller and an aerodynamically-designed streamline-shape fuselage is presented in [19]. A single blade spinning rotor-craft with two tilted rotors is presented in [20] and a transformable vehicle, also known as THOR, which transforms from a fixed-wing aircraft to a spinner can be found in [21].

Fault tolerant control of multicopters in case of partial or complete failure of actuators have become an area of interest among researchers. For example, feedback linearization approach is used in [22] to stabilize a quadcopter after complete loss of one propeller. Stability and control of quadcopters experiencing one, two or three rotor failures are presented in [23], however all propellers have parallel axes of rotation

and the effects of rotation of center of mass of the propellers on their performance are not investigated. To increase reliability by redundancy, quadcopters with tilting rotors, hexacopters and octacopters are introduced which are capable of maintaining stable flight despite losing one to four actuators [24], [25], [26], however they are not optimal in terms of power consumption or stability. Emergency landing for a quadcopter with one rotor failure in an environment without obstacles can be found in [27] where the landing location is known and path planning is not discussed.

An emerging area of research in multi-rotor UAVs falls into finding a landing spot and planning a safe trajectory towards it in case of rotor failure. While there is a huge body of literature on trajectory planning for quadcopters, [28], [29], [30], [31], the work done on extending this to a situation where there is a rotor failure is scarce.

1.2   Motivations and Contributions

Quadcopters with fixed rotors fall under the under-actuated and non-holonomic flying machine categories. Adoption of a larger number of rotors and/or adding the tilting effect on them for on-the-fly thrust vectoring can lead to fully-actuated holonomic machines at the cost of making them mechanically more complicated and less power efficient. There have been some studies on: (i) building UAVs using variable-pitch blades [32]; (ii) configuring rotors to yield non-parallel thrust vectors [33], [34], [35]; (iii) designing multi-copter UAVs with rotors that can tilt on the fly [24]; and (iv) building multi-copter UAVs with rotors fixedly mounted with an angle with respect to the fuselage [36]. However, very little attention has been given

to calculating the optimal configuration in quadcopters with fixed rotors for highest static and dynamic stability. In this thesis, we attempt to look at all possible controllable configurations for a quadcopter with fixed rotors and analyze their stability attributes in a quantitative and analytical fashion for the first time. We also provide a unified dynamic model for all the possible configurations from which special cases can be deducted.

Despite the unprecedented progress in the development of UAVs (especially multicopters) in recent years, two major issues, namely safety and endurance, still remain of main challenges. These vehicles are prone to having different types of failure in the system such as partial or complete loss of motors or propellers, collision with obstacles or other vehicles and power outage. Since they are becoming an inevitable part of our everyday life, safety becomes one of the key factors in designing such vehicles. Our goal is to propose a complete solution including modeling, real-time control and planning for emergency landing of quadcopters in case of a rotor failure.

This thesis also presents a framework for emergency landing of a quadcopter in case of a rotor failure. As mentioned in the previous section, in the literature, typically, the thrust force and moment generated by the propeller is assumed to be proportional to the square of its angular velocity and the effects of freestream on its performance is usually neglected by assuming small freestream velocities. However, this model is not valid in high speed flight and its accuracy deteriorates as flight speed increases. Therefore, based on *blade element theory* [37], a complete mathematical model for the propeller in presence of high speed freestream is derived which results in defining

a specific configuration of quadcopters by adding a tilting and a dihedral angle to the rotors thrust vector, which leads to the minimum power consumption in hovering and also trajectory tracking in case of a rotor failure. Hover solution for different configurations is calculated and a comparison in terms of power consumption amongst them is presented. For the configuration with minimum power consumption, cascaded control strategy is used to control attitude and position of the vehicle and nonlinear simulations validating the results are presented.

For completing the landing, first an algorithm is proposed to find the best landing spot in a given map of the environment where obstacles are represented by cuboids. Two parameters are used to define a cost function to find the optimal landing spot in the given map: (i) finding the safest landing spot with the largest clearance from the obstacles; and (ii) finding an optimal trajectory towards the landing spot. To properly define the clearance from obstacles, *Generalized Voronoi Diagram* (GVD) is used. For all points on the GVD, the one with minimum cost is selected as the landing spot. A finite horizon is selected in generating the GVD. The boundary of this horizon is estimated based on the total cost-to-go based on the power requirement. Furthermore, due to the size and dimensionality of the search space, an RRT*-type randomized motion planning strategy is adopted that can generate optimal trajectories on the fly in real time. In the end, using nonlinear simulations and the designed controller, the results of following the path and performing emergency landing are evaluated.

In the realm of highly under-actuated UAVs and towards designing simpler flying vehicles, this thesis also investigates about the optimal design of a highly under-

actuated and simple spinning UAVs with a streamline-shape fuselage having only two rotors that can provide an optimal solution for hovering while having the best trajectory tracking performance for the first time.

A comprehensive dynamic model of the spinning UAV with two rotors positioned at an offset from the fuselage's COM is developed considering the *blade element theory*. This dynamic model is then used to find the optimal configuration, i.e., optimal aerodynamic characteristics of the rotor and the streamline-shape fuselage for inducing the largest lift and smallest drag simultaneously. More specifically, two possible configurations are explored: (1) a symmetric configuration, in which the rotors are positioned at the same distance from the fuselage's COM but in the opposite directions along y-axis and having opposite tilting angles about the y-axis, and (2) an asymmetric configuration, in which the rotors are positioned on top of each other with different heights and with an offset w.r.t the fuselage's COM. From this point on, the first configuration is called "bispinner" and the second one is called "monospinner".

Furthermore, equilibrium states or hover solutions for both configurations are found and a linear time-invariant control strategy is developed to control attitude and position of the vehicle. In addition, an optimization problem is defined and optimal configurations that yield the most efficient in-position hovering and trajectory tracking for both configurations are formulated and design guidelines are provided. In equilibrium, a *pseudo* in-place hovering is achieved in which case yawing and precession speeds of the spinner will not be zero, but bounded. Furthermore, for the

7

first time, it is shown that power consumption for the flight can be further reduced by introducing a tilting angle between the rotor and the fuselage's principle axis.

In summary, the following enlists major contributions of this thesis:

- Modeling the effects of the freestream velocity on propeller's thrust forces and moments

- Complete mathematical modeling of a spinning UAV incorporating all the gyroscopic moments and cross-coupling of angular momentum in the system as well as considering a streamline-shape fuselage.

- Introducing optimal configurations for quadcopters in terms of stability and maneuverability and using dihedral and twist angles of the rotors

- Fault tolerant control of a quadcopter with tilted rotors and with a rotor failure

- Optimal-power hover solution of a quadcopter with a rotor failure

- Using Generalized Voronoi Diagram (GVD), an algorithm to find the best landing spot with the largest clearance from the obstacles is proposed which leads to finding an optimal trajectory for emergency landing

- Using RRT*-type randomized motion planning algorithm an optimal trajectory towards the landing spot is planned and tracked by the vehicle for landing

- Introducing the tilting angle between the rotors and fuselage's principle axis in spinning UAVs and investigating its effects on power consumption and flight performance

- Presenting optimal configurations for spinning UAVs that would yield the most efficient design for hovering and trajectory tracking along with providing design guidelines

2

Multi-rotor UAV Modeling with Revised Propeller Dynamics

This chapter presents mathematical modeling for multi-rotor UAVs. We begin with presenting a mathematical model of thrust force and moments of a propeller in presence of freestream, this proposed propeller model is used to derive equations of motion of a quadcopter with angled thrust vectors. Also equations of motion of a spinning UAV with two rotors and streamline-shape fuselage.

Throughout the thesis, matrices are represented by straight boldface letters and all vectors are represented by italicized boldface letters. For example, rotation matrix from frame i to frame j is represented by $^{j}\mathbf{R}_i$. In addition, the term $^{I}\boldsymbol{\omega}_p$ denotes $\boldsymbol{\omega}$ belongs to p and is expressed in frame I. Angular velocity vector of the vehicle is represented by $\boldsymbol{\omega}_B = (p, q, r)^T$ where p, q and r are roll, pitch and yaw rates

respectively. Also, 2-Norm of $\boldsymbol{\omega}$ is represented by $\|\boldsymbol{\omega}\|$ and absolute value of s is shown by $|s|$.

2.1 Propeller Model in Presence of Freestream

Freestream velocity may affect propeller's performance depending on its direction and magnitude. Generally, these effects could change propeller's performance in two ways: i) changing the effective angle of attack of the blades; and ii) changing the local airflow velocity over the blades. The former effect is caused when there is a freestream with its velocity vector parallel to the angular velocity vector of the propeller while the latter is caused by any freestream with its velocity vector perpendicular to the angular velocity vector of the propeller. Studying these effects not only helps us to derive a more realistic mathematical model for multi-rotors but also helps to find more stable and power-optimal configurations for such vehicles.

Suppose we have a propeller turning at angular velocity $\boldsymbol{\omega}_p$ as expressed in a frame attached to its COM as shown in Fig. 2.1. The propeller has two blades of radius R_b and is assumed to have constant chord c. For simplicity, first, we assume there is an almost uniform freestream with velocity vector $\boldsymbol{V}_{\infty_1}$, as shown in blue in Fig. 2.1, which is parallel to the y-axis.

Consider a blade element (small hashed area in Fig. 2.2) of length c and differential width dr_b where r_b is the distance of the blade element from the root of the blade. As shown in Fig. 2.2, the rotation of the blade generates relative air flow velocity with magnitude $r_b\|\boldsymbol{\omega}_p\|$, over each blade element. As the propeller is turning, the
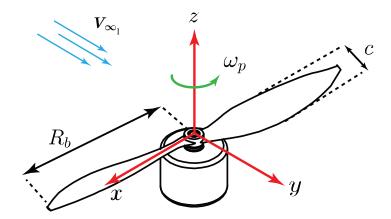
Fig. 2.1. Schematic of a propeller with a frame attached to its COM.

relative air flow velocity over the blade element could either be increased or decreased depending on the azimuth angle of the blade and direction of the freestream velocity. The azimuth angle ψ_p is defined as the angle between the blade and the direction of $\boldsymbol{V}_{\infty_1}$. Therefore, the resultant relative air flow velocity over each blade element can be written as:

$$v = r_b \|\boldsymbol{\omega}_p\| + \|\boldsymbol{V}_{\infty_1}\| \sin \psi_p \tag{2.1}$$
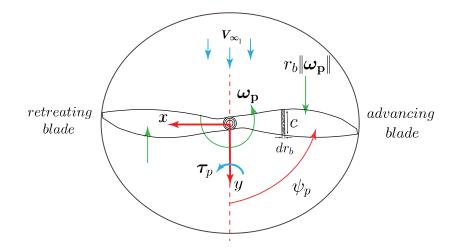
Fig. 2.2. A propeller in presence of freestream.

In Fig. 2.2, for the advancing blade ($0 \leq \psi_p \leq \pi$), freestream velocity increases the relative air flow velocity over the blade and for the retreating blade ($\pi \leq \psi_p \leq 2\pi$), it decreases the relative air flow velocity. The changes in the relative air flow velocity with azimuth angle affects the overall thrust of the propeller and it generates a moment in the direction of the freestream velocity as shown in blue.

Therefore, using (2.1) and according to *Blade Element Theory*, thrust force and moments of each blade element can be calculated as follows:

$$df_p = \frac{1}{2}\rho_a c C_L v^2 dr_b \tag{2.2}$$

$$d\tau_{d_p} = \frac{1}{2}\rho_a c C_D v^2 r_b dr_b \tag{2.3}$$

$$d\tau_p = \frac{1}{2}\rho_a c C_L v^2 r_b \sin\psi dr_b \tag{2.4}$$

where ρ_a represents air density and C_L and C_D are the lift and drag coefficient of the airfoil of the blade respectively. Also, f_p represents thrust force of the blade element, τ_{d_p} represents the moment due to drag force of the blade element and τ_p represents the moment due to change in thrust force with respect to the azimuth angle of the blade.

By integrating (2.2), (2.3) and (2.4) over blade radius r_b and azimuth angle ψ_p, average thrust force and the average moments for one blade as functions of freestream velocity and angular velocity of the propeller can be calculated as follows:

13

$$f_p = \frac{1}{2}\rho_a c C_L \left(\frac{2R_b^3}{3} \|\boldsymbol{\omega}_p\|^2 + \|\boldsymbol{V}_{\infty_1}\|^2 R_b \right) \tag{2.5}$$

$$\tau_{d_p} = \frac{1}{4}\rho_a c C_D \left(R_b^4 \|\boldsymbol{\omega}_p\|^2 + \|\boldsymbol{V}_{\infty_1}\|^2 R_b^2 \right) \tag{2.6}$$

$$\tau_p = \frac{1}{2}\rho_a c C_L R_b^3 \|\boldsymbol{\omega}_p\| \|\boldsymbol{V}_{\infty_1}\| \tag{2.7}$$

Note that by assuming zero freestream velocity, equations (2.5), (2.6) and (2.7) yield the simplified model for thrust force and moments of a propeller which is widely used in the literature (i.e., [4], [18], [23], [29]).

Using the proposed model, simulation results for two complete turns of a propeller with angular velocity $\|\boldsymbol{\omega}_p\| = 900$ rad/s in presence of freestream velocity is presented in Fig. 2.3. Note that the direction of rotation and freestream velocity are the same as those in Fig. 2.2. The remaining parameters of the simulations are as follows: $c = 0.03$ m, $C_L = 1.022$, $C_D = 0.01$, $R_b = 0.08$ m and $\rho_a = 1.225$ kg/m^3. In Fig. 2.3, the top plot presents variations of thrust force with respect to blade azimuth. The red color represents the thrust force when $\|\boldsymbol{V}_{\infty_1}\| = 0$, which is constant, meaning that the relative air flow velocity over the blade element is constant for all azimuth angles. The blue color, represents thrust force of the propeller as a function of azimuth angle when freestream velocity is nonzero, $\|\boldsymbol{V}_{\infty_1}\| = 10$ m/s. Comparing both scenarios, it can be seen that for nonzero freestream velocity and for $0 \leq \psi_p \leq \pi$ thrust force is increased while for $\pi \leq \psi_p \leq 2\pi$ thrust force is decreased which is due to higher relative air flow velocities on the advancing blade than that over the retreating blade. The yellow color shows the average of thrust force of the propeller when $\|\boldsymbol{V}_{\infty_1}\| = 10$

m/s. Results show that in presence of nonzero freestream velocity the average thrust force of the propeller increases.
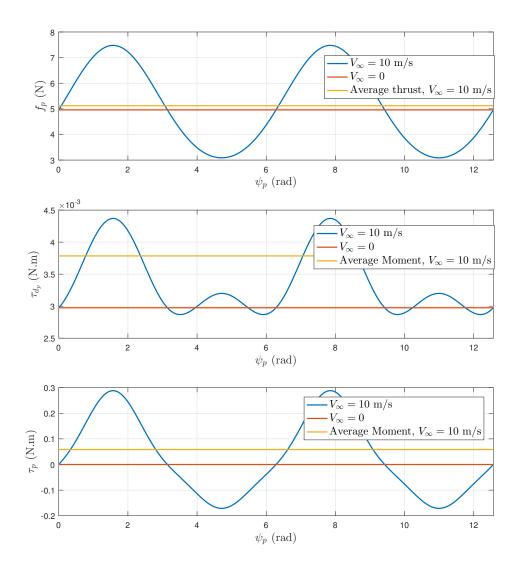
Fig. 2.3. Simulation results for thrust force and moments of a propeller in presence of freestream.

The middle and bottom plots in Fig. 2.3 present variations of the moments due to drag and freestream (τ_{d_p} and τ_p) versus azimuth angle respectively. The red color

15

represents the moment when $\|\boldsymbol{V}_{\infty_1}\| = 0$ m/s, blue color represents variations of moment in presence of freestream velocity $\|\boldsymbol{V}_{\infty_1}\| = 10$ m/s and the yellow color represents the average moment of the propeller when $\|\boldsymbol{V}_{\infty_1}\| = 10$ m/s.

To continue investigating the effects of freestream on propeller's performance, as shown in Fig. 2.4, the freestream velocity vector, $\boldsymbol{V}_{\infty_2}$, is parallel to the angular velocity vector of the propeller, $\boldsymbol{\omega}_p$, as expressed in the frame attached to it.
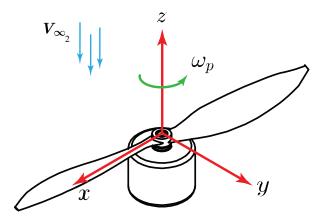
Fig. 2.4. Propeller in presence of freestream. The freestream velocity vector $\boldsymbol{V}_{\infty_2}$ is assumed to be parallel with the angular velocity vector of the propeller $\boldsymbol{\omega}_p$.

Suppose the propeller is turning at angular velocity $\boldsymbol{\omega}_p$ as shown in Fig. 2.5. In absence of freestream, there will be an airflow velocity vector $r_b\boldsymbol{\omega}_p$ over each blade element as shown in green. Also, for each blade element, the angle of attack (AOA) Θ is defined as the angle between the chord of the blade element and the local airflow velocity vector $r_b\boldsymbol{\omega}_p$.

Now, consider an almost uniform freestream with velocity vector $\boldsymbol{V}_{\infty_2}$ in the positive direction of z-axis as shown in blue in Fig. 2.5 top. As shown, the freestream
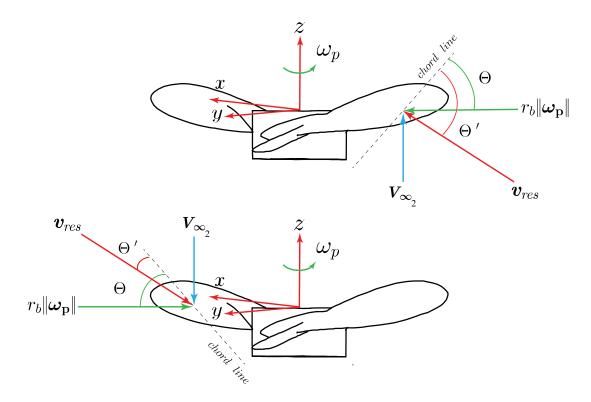
Fig. 2.5. Propeller in presence of freestream. The freestream velocity vector $\boldsymbol{V}_{\infty_2}$ is assumed to be parallel with $\boldsymbol{\omega}_p$. On top, $\boldsymbol{V}_{\infty_2}$ is the positive direction of z-axis and in bottom it is assumed to be in the opposite direction.

changes the direction and magnitude of the resultant airflow velocity over the blade element as shown in red in Fig. 2.5 top. Therefore, the new angle of attack Θ', in presence of freestream is greater than that in absence of freestream ($\Theta' \geq \Theta$).

However, if the freestream velocity vector is in the negative direction of z-axis (see Fig. 2.5 bottom), it changes the direction and magnitude of the resultant airflow velocity vector such that it decreases the effective angle of attack ($\Theta' \leq \Theta$).

The importance of studying AOA is because it directly affects the lift coefficient of the blade element and consequently affects the thrust force generated by the pro-

peller. At low speed flight (subsonic) and assuming small angles, the lift coefficient C_L changes almost linearly with AOA which can be written as follows [37]:

$$\frac{\Delta C_L}{\Delta \Theta} = \sigma \tag{2.8}$$

where σ is a constant which is determined through experiments in wind tunnel. From (2.2), any increase (decrease) in C_L increases (decrease) the thrust force of the blade element. Therefore, in summary the results are as follows:

- Any freestream with positive (negative) z-component velocity (expressed in the propeller's frame) increases (decreases) the AOA which increases (decreases) the thrust force.

Furthermore, to formulate the changes in thrust force of the propeller, first we can write the changes in AOA of each blade element as follows:

$$\Delta \Theta = \Theta - \Theta' = \arctan \frac{\|\boldsymbol{V}_{\infty_2}\|}{\|r_b \boldsymbol{\omega}_p\|} \tag{2.9}$$

Finally, using (2.2), (2.8) and (2.9), the changes in thrust force of the propeller can be written as follows:

$$\Delta f_p = \frac{1}{4}\rho_a c \sigma R_b^2 \|\boldsymbol{V}_{\infty_2}\| \|\boldsymbol{\omega}_p\| \tag{2.10}$$

From (2.10), it can be seen that the changes in thrust force is proportional to the magnitude of the freestream velocity vector $\boldsymbol{V}_{\infty_2}$.

In summary, we presented the significance of the effects of freestream on performance of propellers. We formulated these effects as functions of propeller parameters and also the parameters of the freestream. Table 2.1 presents all parameters involved in the proposed propeller model. We continue this chapter by presenting mathematical modeling of two types of multi-rotor UAVs, namely quadcopters and spinners, using the proposed propeller model.

Table 2.1.
Important parameters for modeling of propellers.

$\boldsymbol{\omega}_p$	angular velocity vector of the propeller
Θ	angle of attack
$C_L,\ C_D$	lift and drag coefficients of the airfoil
$\boldsymbol{V}_\infty$	freestream velocity vector
σ	slope of C_L vs Θ curve for the airfoil
R_b	blade radius of the propeller
c	chord of the blade
r_b	distance from blade element to root of the blade
ρ_a	air density
f_p	thrust force of the propeller
τ_{d_p}	moment of the propeller due to drag
τ_p	moment of the propeller due to asymmetrical lift distribution

2.2   Dynamic Model of Quadcopters with Angled Thrust Vectors

This section presents mathematical modeling of quadcopters with angled thrust vectors by utilizing the proposed model of the propeller in the previous section. Literature pertinent to the mathematical modeling of quadcopters and their flight control is vast. In our derivation, we assume a full model of the gyroscopic moments and cross-coupling of angular momentum in the system. More specifically, we derive the dynamic model of quadcopters assuming that: i) the thrust vector for each rotor would make a non-zero angle with the vertical axis (i.e., the sagittal suture) of the quadcopter; and ii) the center of mass (COM) of the quadcopter does not lie on the same plane where the center-of-mass of all motors lie on (blue plane shown in Fig. 2.6). However, we still assume that the quadcopter under study has two axes of congruency.

The angle between the thrust vector of each rotor and the vertical axis of the fuselage is further divided into: i) the dihedral angle; and ii) twist (i.e., lateral tilting) angle (Figs 2.7 and 2.8). We assume that the central hub of all four rotors lie on a flat horizontal plane (blue plane in Fig. 2.6), called flat plane from this point on, from which the location of the COM is referenced (i.e., the COM can be either above, below, or right on this plane).

The dynamic model developed in this section will, therefore, have three additional terms in comparison to that in the flat quadcopters (this is the term used for the original quadcopters, where the COM and the rotor hubs are all on the same plane),
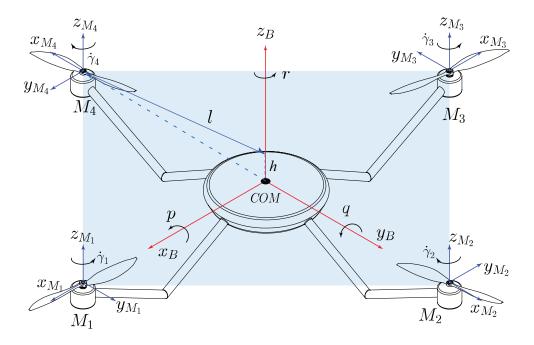
Fig. 2.6. Quadcopter in "+" configuration. Body frame is shown in blue and is attached to the center-of-mass of the quadcopter. A frame, shown in blue, is attached to each motor in order to determine orientation of the motors with respect to body frame. Motors are located at distance l and h from z-axis and x-y plane of the body frame respectively.

as: dihedral angle β_i, twist angle α_i, and the distance between the COM and the flat plane h (please note that h could take positive and negative values, measured in z-direction of the body frame). In existing flat model of quadcopters one has: $\beta_i = \alpha_i = d = 0$. We use Newton's method for deriving the dynamic model of the quadcopter. Also, without the loss of generality, we assume a "+" configuration.

The body frame $^BO - {}^Bx^By^Bz$ (red color in Fig. 2.6) is attached to the center of mass of the vehicle. Four frames named $^{M_i}O - {}^{M_i}x^{M_i}y^{M_i}z$ (blue color in Fig. 2.6) are attached to motors. Motors are turning with angular velocities $\dot{\gamma}_i$ $(i = 1, 2, ..., 4)$ about z_{M_i}-axis. Position of the vehicle is expressed in the inertial frame I. Also $^B\boldsymbol{\omega}_{p_i,I}$
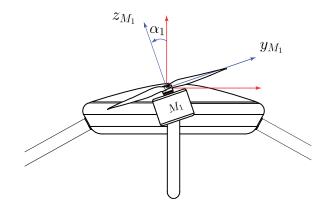
Fig. 2.7. Twist angle α_1 about the x-axis of the motor frame M_1.
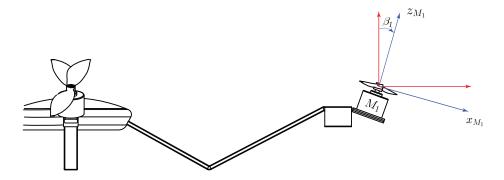
Fig. 2.8. Dihedral angle β_1 about the y-axis of the motor frame M_1.

indicates that $\boldsymbol{\omega}$ belongs to the ith propeller with respect to an inertial frame I and is expressed in the body frame B. Finally, we represent a rotation matrix about axis A by angle θ as $\mathbf{R}_A(\theta)$.

Orientation of the body frame with respect to the inertial frame can be captured by the rotation matrix ${}^I\mathbf{R}_B$ from body frame to inertial frame. This rotation matrix is a function of time and its evolution in time can be obtained as follows:

$$
{}^I\dot{\mathbf{R}}_B = {}^I\mathbf{R}_B \, \mathrm{sk}({}^B\boldsymbol{\omega}_{B,I})
\tag{2.11}
$$

where sk($^B\boldsymbol{\omega}_{B,I}$) is the skew-symmetric matrix of angular velocity of the body with respect to the inertial frame as expressed in the body frame $^B\boldsymbol{\omega}_{B,I} = [p, q, r]^T$.

Likewise, the orientation of each motor frame M_i can be obtained with respect to the body frame. First the position of the origin of frame M_i with respect to body frame from the origin of the body frame can be written as:

$$^B\boldsymbol{O}_{M_i} = \mathbf{R}_{z_B}((i-1)\frac{\pi}{2}) \begin{bmatrix} l \\ 0 \\ h \end{bmatrix} , \quad (i = 1, 2, ..., 4) \tag{2.12}$$

Since we are using a quadcopter in "+" configuration, we assume that the motors are evenly distributed by angle $\frac{\pi}{2}$ about z_B-axis. Therefore, the transformation from frame M_i to body frame is obtained as follows:

$$^B\mathbf{R}_{M_i} = \mathbf{R}_z((i-1)\frac{\pi}{2})\mathbf{R}_y(\beta_i)\mathbf{R}_x(\alpha_i) , \quad (i = 1, 2, ..., 4) \tag{2.13}$$

Suppose the quadcopter is consisted of several rigid bodies and it is considered to be symmetric about its axes of rotation. Because of the symmetry, the inertia tensor of the vehicle, $\mathbf{I}^B$, will be diagonal and is expressed in the body frame. We also assume that the moment of inertia of the propellers, $\mathbf{I}^p$, are very small compared to $\mathbf{I}^B$. We can neglect drag force in angular motion of the body by assuming very

small angular velocities. Considering these simplifying assumptions, the rotational

motion is governed by the following equation:

$$\boldsymbol{\tau} = \mathbf{I}^B\dot{\boldsymbol{\omega}}_{B,I} + \sum_{i=1}^{4}\mathbf{I}^{pB}\dot{\boldsymbol{\omega}}_{p_i} + {}^B\boldsymbol{\omega}_{B,I} \times \left(\mathbf{I}^B\boldsymbol{\omega}_{B,I} + \sum_{i=1}^{4}\mathbf{I}^{pB}\boldsymbol{\omega}_{p_i}\right) \qquad (2.14)$$

where ${}^B\boldsymbol{\omega}_{p_i}$ is the angular velocity vector of the ith propeller with respect to the

inertial frame as expressed in the body frame which can be written as follows:

$$ {}^B\boldsymbol{\omega}_{p_i} = {}^B\mathbf{R}_{M_i}[0,0,\dot{\gamma}_i^2]^T \qquad (2.15)$$

where $\dot{\gamma}_i$ is the angular velocity of the ith propeller about z-axis of frame M_i. In

(2.14), $\boldsymbol{\tau}$ is the external moment generated by thrust forces and the reaction from

propellers plus the drag of the fuselage expressed in the body frame $(\boldsymbol{\tau}_{d_B})$. Thrust

force and reaction moment of each propeller as expressed in the frame M_i, can be

calculated using the proposed propeller model in the previous section. The external

moment $\boldsymbol{\tau}$ can be written as follows:

$$\boldsymbol{\tau} = \boldsymbol{\tau}_{d_B} + \sum_{i=1}^{4}\left({}^B\boldsymbol{O}_{M_i} \times {}^B\mathbf{R}_{M_i}{}^{M_i}\boldsymbol{f}_{p_i} + {}^B\mathbf{R}_{M_i}\left({}^{M_i}\boldsymbol{\tau}_{p_i} + {}^{M_i}\boldsymbol{\tau}_{d_{p_i}}\right)\right) \qquad (2.16)$$

The position of the vehicle in inertial frame is shown by Cartesian coordinates $\boldsymbol{d} =$

$[d_1, d_2, d_3]^T$. Therefore, the equation governing translational motion can be written

as follows:

$$m\ddot{\boldsymbol{d}} = {}^{I}\mathbf{R}_B \sum_{i=1}^{4} \left({}^{B}\mathbf{R}_{M_i}{}^{M_i}\boldsymbol{f}_{p_i} \right) + m\boldsymbol{g} \qquad (2.17)$$

where m is total mass of the vehicle and $\boldsymbol{g}$ is gravitational acceleration vector expressed in the inertial frame. Note that we assume small translational velocities, therefore the drag forces due to translational motion can be neglected in (2.17).

2.3 Dynamic Model of Spinning UAVs with Streamline-shape Fuselage

In this section, dynamic model of a spinning UAV including aerodynamic model of a propeller in presence of freestream velocity is presented for the first time followed by introducing two specific configurations namely, monospinner and bispinner.

Fig. 2.9 shows a vehicle of mass m with a streamline-shape fuselage. Two rotors are positioned at $\boldsymbol{p}_1 = (0, l_1, h_1)$ and $\boldsymbol{p}_2 = (0, l_2, h_2)$ in the y-z plane of the body frame, B, as shown in blue. The ith rotor can rotate independently about the y-axis of the body frame by angle δ_i with rotations in the direction of positive y-axis resulting in positive angles. A propeller is attached to each rotor turning with angular velocity $\omega_{p_i}\boldsymbol{e}_{p_i}$ where ω_{p_i} is the magnitude of angular velocity and $\boldsymbol{e}_{p_i}$ is the unit vector determining the direction of rotation of the ith propeller in the body frame. Also, the angular velocity of the fuselage with respect to the inertial frame as expressed in the body frame is represented by $\boldsymbol{\omega}_B = (p, q, r)^T$. Furthermore, it is assumed the propeller has two blades with chord c_p and radius R_p. The fuselage is to be streamline-shape,

25

aerodynamic and similar to the propeller with four blades with chord c_B and radius R_B. It is also assumed that the chord is constant throughout the radius of the blades.
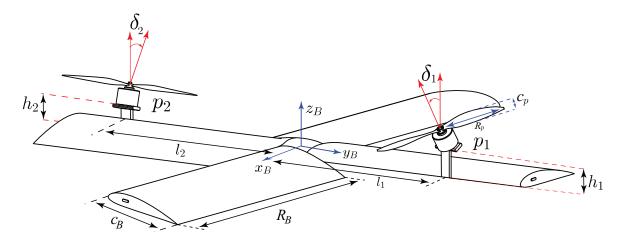
Fig. 2.9. A spinning UAV with two rotors and streamline-shape fuselage.

The moment of inertia matrix of the propeller is approximated by the moment of inertia of a disk as expressed in the body frame by $\mathbf{I}^p = \mathrm{diag}(I^p_{xx}, I^p_{yy}, I^p_{zz})$. The moment of inertia matrix of the fuselage is also represented by a diagonal matrix $\mathbf{I}^B = \mathrm{diag}(I^B_{xx}, I^B_{yy}, I^B_{zz})$. Furthermore, it is assumed that the fuselage is symmetric such that $I^B_{xx} = I^B_{yy}$. In addition, the position of the vehicle expressed in inertial frame is denoted by $\boldsymbol{d} = (d_1, d_2, d_3)$. The equations of motion can now be written as follows:

$$\boldsymbol{\tau} = \mathbf{I}^B \dot{\boldsymbol{\omega}}_B + \sum_{i=1}^{2} \mathrm{I}^p \dot{\boldsymbol{\omega}}_{p_i} + \mathrm{sk}(\boldsymbol{\omega}_B)\Big(\mathbf{I}^B \boldsymbol{\omega}_B + \sum_{i=1}^{2} \mathrm{I}^p(\boldsymbol{\omega}_{p_i} + \boldsymbol{\omega}_B)\Big) \tag{2.18}$$

$$\boldsymbol{\tau} = \sum_{i=1}^{2} \Big(\boldsymbol{p}_i \times \boldsymbol{f}_{p_i}\Big) + \sum_{i=1}^{2} \boldsymbol{\tau}_{d_{p_i}} + \boldsymbol{\tau}_{d_B} + \sum_{i=1}^{2} \boldsymbol{\tau}_{p_i} \tag{2.19}$$

$$m\ddot{\boldsymbol{d}} = {}^{I}\mathbf{R}_B\Big(\sum_{i=1}^{2} \boldsymbol{f}_{p_i} + \boldsymbol{f}_B\Big) + m\boldsymbol{g} \tag{2.20}$$

26

In the right hand side of (2.18), the first two terms represent the moments due to angular accelerations of the fuselage and propellers. The third term represents cross-coupling of angular momentum due to rotation of the fuselage and propellers and $\text{sk}(\boldsymbol{\omega}_B)$ represents the skew-symmetric matrix of the angular velocity vector of the fuselage. In the right hand side of (2.19), the first term represents the moment due to propeller's thrust force about the center of mass of the vehicle, the second term represents the sum of reaction moments of the propellers, the third term is the moment due to drag of the fuselage and the last term is the sum of moments due to asymmetrical lift distribution over the advancing and retreating blades of the propellers.

In (2.20), $\boldsymbol{f}_B$ represents thrust force generated by the streamline-shape fuselage, $\boldsymbol{g}$ is the gravitational acceleration and ${}^I\mathbf{R}_B$ is the rotation matrix from body frame to inertial frame. Since the fuselage is turning with yaw rate r about the z-axis of the body frame, it generates a thrust force $\boldsymbol{f}_B$ along with a moment $\boldsymbol{\tau}_{d_B}$ due to its aerodynamic drag, in the direction of z-axis of the body frame. These can be calculated using *Blade Element Theory* as follows:

$$\boldsymbol{f}_B = \frac{1}{3}\rho_a c_B C_{L_B} R_B^3 r^2\, \boldsymbol{e}_{\boldsymbol{f}_B} \tag{2.21}$$

$$\boldsymbol{\tau}_{d_B} = \frac{1}{4}\rho_a c_B C_{D_B} R_B^4 r^2\, \boldsymbol{e}_{\boldsymbol{\tau}_{d_B}} \tag{2.22}$$

where ρ_a is the air density and C_{L_B} and C_{D_B} are lift and drag coefficients of the fuselage respectively. Also, $\boldsymbol{e}_{\boldsymbol{f}_B}$ and $\boldsymbol{e}_{\boldsymbol{\tau}_{d_B}}$ represent unit vectors showing the direction

of thrust force and moment of the fuselage respectively. In both propellers and the fuselage, *NACA 4415* airfoil is used where its lift and drag coefficients, C_L and C_D respectively, as a function of angle of attack Θ can be obtained as follows [38]:

$$C_L = 0.1\Theta + 0.5 \qquad C_D = 0.006\Theta + 0.04 \tag{2.23}$$

Note that (2.23) is only valid for $-10° \leq \Theta \leq 10°$.

2.3.1 Effects of Freestream in Spinning UAVs

In this section, based on the propeller model proposed in this chapter, we derive equations to determine the effective angle of attack, thrust force and moments of the propellers in a spinning UAV.

Suppose a propeller is turning with angular velocity vector $\boldsymbol{\omega}_p$ as shown in Fig. 2.10. The rotor is positioned at distance l from COM of the vehicle and is tilted by angle δ about the y-axis of the body frame and the fuselage is spinning at yaw rate r about the z-axis of the body frame as shown in Fig. 2.10. As the vehicle is spinning, the propeller experiences an almost uniform freestream expressed in the body frame as:

$$^B\boldsymbol{V}_\infty = (rl, 0, 0)^T \tag{2.24}$$

Because of the tilting angle δ, this freestream will have vertical and horizontal components in the propeller's plane. According to *Blade Element Theory*, the vertical component changes the effective angle of attack of the blades as follows:

$$\Theta_{eff} = \theta + \arctan \frac{rl \sin \delta}{|R_p(\|\boldsymbol{\omega}_p\| + r \cos \delta)|} \qquad (2.25)$$

where θ is the pitch angle of the blade, R_p is the blade radius and $(\|\boldsymbol{\omega}_p\| + r \cos \delta)$ is the resultant angular velocity of the propeller with respect to the inertial frame. Equation (2.25) indicates that depending on the sign of tilting angle and the yaw rate, the effective angle of attack could be either increased or decreased.
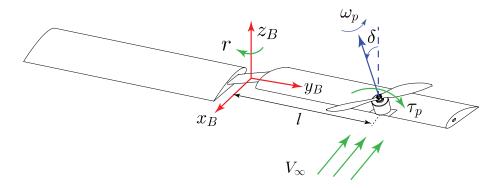
Fig. 2.10. Effects of freestream on propeller's performance in a spinning UAV.

We have shown that the horizontal component of freestream velocity (perpendicular to the angular velocity vector of the propeller) changes the local airflow velocity over each blade element. Also, the vertical component of freestream velocity (parallel to the angular velocity vector of the propeller) changes the effective angle of attack of the blade elements. Therefore, considering these changes and according to equations (2.5), (2.6) and (2.7), thrust force and the moments generated by the propeller can be written as follows:

$$\boldsymbol{f}_p = \rho_a c_p C_{L_p} \left(\frac{R_p^3 \|\boldsymbol{\omega}_p\|^2}{3} + \frac{R_p^3 r^2 \cos^2 \delta}{3} + \frac{R_p r^2 l^2 \cos^2 \delta}{2} + \frac{2R_p^3 r \|\boldsymbol{\omega}_p\| \cos \delta}{3} \right) \boldsymbol{e}_{\boldsymbol{f}_p} \quad (2.26)$$

29

$$\boldsymbol{\tau}_{d_p} = \rho_a c_p C_{D_p} \left(\frac{R_p^4 \|\boldsymbol{\omega}_p\|^2}{4} + \frac{R_p^4 r^2 \cos^2 \delta}{4} + \frac{R_p^2 r^2 l^2 \cos^2 \delta}{2} + \frac{R_p^4 r \|\boldsymbol{\omega}_p\| \cos \delta}{2} \right) \boldsymbol{e}_{\boldsymbol{\tau}_{d_p}} \quad (2.27)$$

$$\boldsymbol{\tau}_p = \rho_a c_p C_{L_p} \left(\frac{R_p^3 \|\boldsymbol{\omega}_p\| r l \cos \delta + R_p^3 r^2 l \cos^2 \delta}{3} \right) \boldsymbol{e}_{\boldsymbol{\tau}_p} \quad (2.28)$$

where $\boldsymbol{e}_{\boldsymbol{f}_p}$, $\boldsymbol{e}_{\boldsymbol{\tau}_{d_p}}$ and $\boldsymbol{e}_{\boldsymbol{\tau}_p}$ are unit vectors expressed in the body frame to determine the directions of propeller's thrust force, reaction moment and the moment due to asymmetrical lift distribution respectively.

Finally, by adding the following constraints to the system, two specific configurations namely monospinner and bispinner, are introduced. The first configuration is achieved when $l_1 = l_2 = l$, $\delta_1 = \delta_2 = \delta$ and h_2 is slightly larger or smaller than h_1 such that the second rotor can be positioned either above or below the first rotor (e.g., $h_2 = 1.1 h_1 = h$) . This configuration is also known as monospinner since the two rotors could be replaced by a single rotor which yields to the simplest possible configuration for a multi-rotor flying vehicle. The second configuration is defined such that $l_2 = -l_1 = l$, $\delta_2 = -\delta_1 = \delta$ and $h_1 = h_2 = h$, also known as bispinner which provides more stability and improved controllability compared to the monospinner.

3

Flight Control

This chapter presents development of flight control strategies for multi-rotor UAVs. We begin with presenting a control strategy for quadcopters with angled thrust vectors. Next, a new control strategy is developed for quadcopters experiencing a rotor failure. In this new control strategy, first a new hover definition is provided and the control strategy is built upon it. The new control strategy is then extended to be utilized in spinning-type UAVs with streamline-shape fuselage. In the end, nonlinear simulation are presented to validate the results.

3.1 Flight Control of Quadcopters with Angled Thrust Vector

This section presents the development of a control strategy for the quadcopter model presented in Section 2.2. We use a nested control structure to control orienta-

tion and position of the vehicle. Suppose we have a quadcopter as shown in Fig. 3.1. The body frame B is shown in red and is attached to the COM of the vehicle. As defined in the previous chapter, we represent the position of the vehicle in the inertial frame with the vector $\boldsymbol{d} = [d_1, d_2, d_3]^T$.
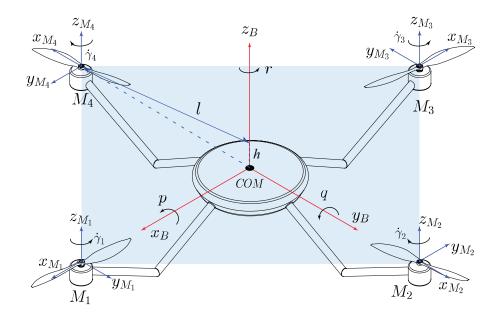
Fig. 3.1. Quadcopter with tilted rotors in "+" configuration. Body frame is shown in blue and is attached to the center-of-mass of the quadcopter.

The orientation of the vehicle (body frame) with respect to the inertial frame is represented by the Euler angles (ϕ, θ, ψ), where ϕ is the roll angle about the x-axis of the body frame, θ is the pitch angle about the y-axis of the body frame and ψ is the yaw angle about the z-axis of the body frame. Therefore, using roll-pitch-yaw rotation sequence, one can find the rotation matrix from body frame to inertial frame as follows [39] (details are shown in Appendix A):

$$
{}^{I}\mathbf{R}_{B} = \begin{bmatrix} c_{\theta}c_{\psi} & s_{\phi}s_{\theta}c_{\psi} - c_{\phi}s_{\psi} & s_{\phi}s_{\psi} + c_{\phi}s_{\theta}c_{\psi} \\[6pt] c_{\theta}s_{\psi} & c_{\phi}c_{\psi} + s_{\phi}s_{\theta}s_{\psi} & c_{\phi}s_{\theta}s_{\psi} - s_{\phi}c_{\psi} \\[6pt] -s_{\theta} & s_{\phi}c_{\theta} & c_{\phi}c_{\theta} \end{bmatrix} \tag{3.1}
$$

where s and c represent sin and cos functions.

In addition, since each rotor has a tilting angle, therefore, according to (2.13), four rotation matrices from motor frames M_i to body frame can be found as follows:

$$
{}^{B}R_{M_1} = \begin{bmatrix} c_{\beta_1} & s_{\alpha_1}s_{\beta_1} & c_{\alpha_1}s_{\beta_1} \\[6pt] 0 & c_{\alpha_1} & -s_{\alpha_1} \\[6pt] -s_{\beta_1} & c_{\beta_1}s_{\alpha_1} & c_{\alpha_1}c_{\beta_1} \end{bmatrix} \tag{3.2}
$$

$$
{}^{B}R_{M_2} = \begin{bmatrix} 0 & -c_{\alpha_2} & s_{\alpha_2} \\[6pt] c_{\beta_2} & s_{\alpha_2}s_{\beta_2} & c_{\alpha_2}s_{\beta_2} \\[6pt] -s_{\beta_2} & c_{\beta_2}s_{\alpha_2} & c_{\alpha_2}c_{\beta_2} \end{bmatrix} \tag{3.3}
$$

$$
{}^{B}R_{M_3} = \begin{bmatrix} -c_{\beta_3} & -s_{\alpha_3}s_{\beta_3} & -c_{\alpha_3}s_{\beta_3} \\[6pt] 0 & -c_{\alpha_3} & s_{\alpha_3} \\[6pt] -s_{\beta_3} & c_{\beta_3}s_{\alpha_3} & c_{\alpha_3}c_{\beta_3} \end{bmatrix} \tag{3.4}
$$

$$
{}^{B}R_{M_4} = \begin{bmatrix} 0 & c_{\alpha_4} & -s_{\alpha_4} \\[6pt] -c_{\beta_4} & -s_{\alpha_4}s_{\beta_4} & -c_{\alpha_4}s_{\beta_4} \\[6pt] -s_{\beta_4} & c_{\beta_4}s_{\alpha_4} & c_{\alpha_4}c_{\beta_4} \end{bmatrix} \tag{3.5}
$$

Now, using (3.1) to (3.5), equations of motion are available in the body frame. Notice that since quadcopters fall in the category of under-actuated robots, only four out of its six degrees of freedom can be directly controlled, three of which being the Euler angles determining orientation of the vehicle and one of which being the altitude of the vehicle. However, the remaining two translational degrees of freedom are controlled indirectly by manipulating roll and pitch angles. In the proposed nested control structure, in the innermost loop, we use proportional and derivative (PD) controller to control the orientation of the vehicle as follows:

$$\tau_\phi = k_{p_\phi}(\phi_d - \phi) + k_{d_\phi}(\dot{\phi}_d - \dot{\phi}) \tag{3.6}$$

$$\tau_\theta = k_{p_\theta}(\theta_d - \theta) + k_{d_\theta}(\dot{\theta}_d - \dot{\theta}) \tag{3.7}$$

$$\tau_\psi = k_{p_\psi}(\psi_d - \psi) + k_{d_\psi}(\dot{\psi}_d - \dot{\psi}) \tag{3.8}$$

where τ_ϕ, τ_θ and τ_ψ are the three components of (2.14) as $\boldsymbol{\tau} = [\tau_\phi, \tau_\theta, \tau_\psi]^T$, k_p and k_d represent proportional and derivative gains of the controller respectively and ϕ_d, θ_d and ψ_d represent the desired values for Euler angles. Normally, the desired values do not experience much changes, therefore, it is safe to assume $\dot{\phi}_d = \dot{\theta}_d = \dot{\psi}_d = 0$ [40]. Also, ψ_d is commanded to the controller and is known a priori.

Furthermore, the rate of change of Euler angles, $\dot{\phi}$, $\dot{\theta}$ and $\dot{\psi}$ can be obtained from the body angular rates of the vehicle $\boldsymbol{\omega}_B = [p, q, r]^T$. First, from (2.14), p, q and r

can be calculated and then using the following kinematic equation, Euler angle rates can be obtained as follows [39]:

$$
\begin{bmatrix} \dot{\phi} \\ \dot{\theta} \\ \dot{\psi} \end{bmatrix} = \begin{bmatrix} 1 & \tan\theta\sin\phi & \tan\theta\cos\phi \\ 0 & \cos\phi & -\sin\phi \\ 0 & \sin\phi/\cos\theta & \cos\phi/\cos\theta \end{bmatrix} \begin{bmatrix} p \\ q \\ r \end{bmatrix} \tag{3.9}
$$

Eventually, by integrating (3.9), Euler angles can be obtained.

To find ϕ_d, θ_d, first we consider the position control problem. Suppose the desired position of the vehicle is to be at $\boldsymbol{d}_d = [d_{x_d}, d_{y_d}, d_{z_d}]^T$ as expressed in the inertial frame. To control the x- and y-components of position, we define a new frame named B_1 which is attached to the COM of the vehicle and its x-y plane is parallel to the x-y plane of the inertial frame and it only can rotate about its z-axis by angle ψ (the yaw angle). It is assumed that the x-axis of B_1 represents the front of the vehicle. We also represent the total thrust force of all propellers with a new variable $\boldsymbol{f}_\Sigma = [f_x, f_y, f_z]^T$ as expressed in the frame B_1. Therefore, to move the vehicle in the x-direction of B_1, we should pitch the nose down by pitch angle θ and generate a force (acceleration) in the x-direction. If we limit pitch and roll angles to accept only small values, one can write the following equation:

$$
f_x = \|\boldsymbol{f}_\Sigma\|\sin\theta \approx \|\boldsymbol{f}_\Sigma\|\theta \tag{3.10}
$$

Afterwards, by controlling the velocity of the vehicle in this direction, using a simple proportional control law, we can calculate the desired force to accelerate the vehicle towards the desired position as follows:

$$f_{x_d} = \|\boldsymbol{f}_\Sigma\|\theta_d = mk_{pv,x}\left(^{B_1}v_{x_d} - {}^{B_1}v_x\right) \tag{3.11}$$

where $^{B_1}v_x$ is the x-component of the velocity vector of the vehicle as expressed in the frame B_1 which can be obtained by integrating (2.17) and transforming the resulting vector to frame B_1. Also, $^{B_1}v_{x_d}$ is the desired x-component of the velocity vector of the vehicle in the frame B_1 which can be calculated by using another proportional control law as follows:

$$^{B_1}v_{x_d} = k_{p,x}\left(^{B_1}d_{x_d} - {}^{B_1}d_x\right) \tag{3.12}$$

where $^{B_1}d_{x_d}$ is the desired x-component of the position vector of the vehicle as expressed in frame B_1 and $^{B_1}d_x$ is the x-component of the position vector of the vehicle by integrating (2.17) twice. Note that $k_{pv,x}$ and $k_{p,x}$ are the proportional gains of the corresponding control law. Finally, by combining (3.10), (3.11) and (3.12), we can calculate the desired pitch angle as follows:

$$\theta_d = \frac{m}{\|\boldsymbol{f}_\Sigma\|}k_{pv,x}\left(k_{p,x}\left(^{B_1}d_{x_d} - {}^{B_1}d_x\right) - {}^{B_1}v_x\right) \tag{3.13}$$

Similarly, the desired roll angle can be calculated as follows:

$$\phi_d = \frac{m}{\|\boldsymbol{f}_\Sigma\|} k_{pv,y}\left(k_{p,y}\left(^{B_1}d_{y_d} - {}^{B_1}d_y\right) - {}^{B_1}v_y\right) \tag{3.14}$$

In addition, the transformation from inertial frame to the frame B_1 can be written as follows:

$$^{B_1}R_I = \begin{bmatrix} \cos\psi & -\sin\psi & 0 \\ \sin\psi & \cos\psi & 0 \\ 0 & 0 & 1 \end{bmatrix} \tag{3.15}$$

In the end, to control the altitude of the vehicle or the z-component of the position vector of the vehicle as expressed either in the inertial frame or the frame B_1, we use another PD controller as follows:

$$\left(f_z - m\|\boldsymbol{g}\|\right) = k_{p,z}(d_{z_d} - d_z) + k_{d,z}(\dot{d}_{z_d} - \dot{d}_z) \tag{3.16}$$

where d_{z_d} represents the desired altitude and d_z represents the altitude of the vehicle calculated from integrating the translational equation of motion. Also, $k_{p,z}$ and $k_{d,z}$ represent proportional and derivative gains of the PD controller of altitude. Fig. 3.2 presents a block diagram of the proposed control structure for a quadcopter with titled rotors. Note that in the control mixing block, all the input moments and forces are converted to angular velocities of the propellers with the help of equations (2.14) and (2.17).
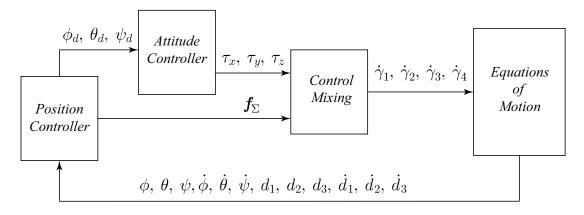
Fig. 3.2. Block diagram of the proposed nested loop control structure for a quadcopter with tilted rotors.

The proposed controller is tested on a vehicle with the following specifications and nonlinear simulation results for position control are presented in Fig. 3.3.

$$m = 0.5 \text{ kg}, \ |\alpha_i| = |\beta_i| = 0.05 \text{ rad}, \ \mathbf{I}^p = \text{diag}([0, 0, 1.5 \times 10^{-5}]) \text{ kg.m}^2$$

$$\mathbf{I}^B = \text{diag}([3.2 \times 10^{-3}, 3.2 \times 10^{-3}, 5.5 \times 10^{-3}]) \text{ kg.m}^2$$
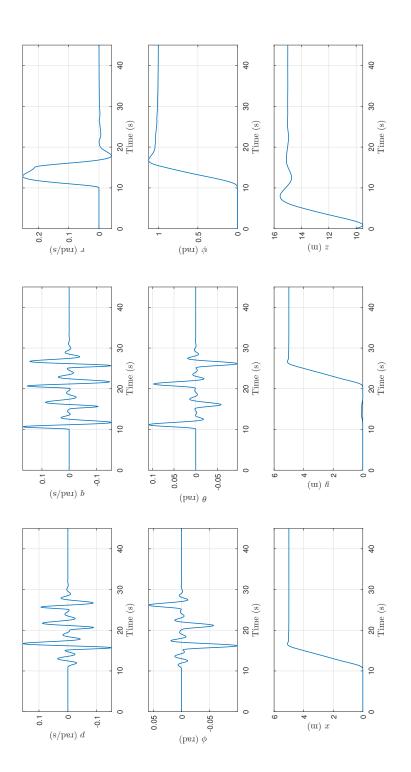
$$h = 0, \ l = 0.17 \text{ m}, \ \rho_a = 1.022 \text{ kg/m}^3, \ c = 0.03 \text{ m}, \ C_L = 1, \ C_D = 0.01$$

$$k_{p_\phi} = k_{p_\theta} = k_{p_\psi} = k_{p,z} = 2, \ k_{d_\phi} = k_{d_\theta} = k_{d_\psi} = k_{d,z} = 1,$$

$$k_{pv,x} = k_{pv,y} = 0.3, \ k_{p,x} = k_{p,y} = 0.1$$

$$\phi_0 = \theta_0 = \psi_0 = 0, \ \boldsymbol{d}_0 = [0, 0, 10]^T \text{ m}, \ \boldsymbol{d}_d = [5, 5, 15]^T \text{ m}, \ \psi_d = 1 \text{ rad}$$

where $\boldsymbol{d}_0$ is the initial position of the vehicle and $\boldsymbol{d}_d$ is its desired position.

Fig. 3.3. Nonlinear simulation results for position control of a quadcopter with tilted rotors.

39

As it can be seen in Fig. 3.3, the proposed simple controller does a good job in tracking the reference values.

3.2 Flight Control of Quadcopters with One Rotor Failure

This section presents development of a control strategy for a quadcopter experiencing a rotor failure. We use the quadcopter model presented in the previous chapter and for simplicity we assume all the tilting angles of the rotors (dihedral and twist angles) and the offset of the COM h are zero. Therefore, the thrust vector of all the propellers will be pointing in the positive direction of the z-axis of the body frame as shown in Fig. 3.4.
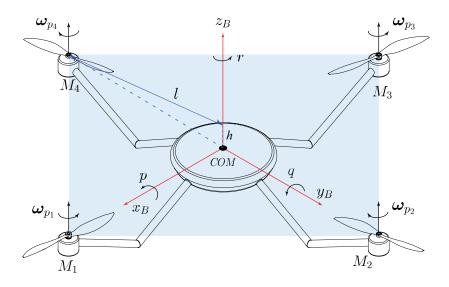
Fig. 3.4. Quadcopter in "+" configuration. All the tilting angles are set to zero.

Generally, in multi-rotor UAVs, hovering is defined as maintaining a position with zero angular and linear velocities. However, in case of one rotor failure in a quadcopter and in order to control the attitude and position of the vehicle, a new

hover definition is required and the old hover solutions no longer hold true. The new hovering is defined as maintaining an altitude while rotating with constant angular velocity about a unit vector that is fixed with respect to the vehicle [18].

Without loss of generality, suppose that motor number 4 (see Fig. 3.4) is failed. Because of the unbalanced moments of the remaining functioning propellers, the vehicle starts rotating about a unit vector $\boldsymbol{n}$ (as expressed in the body frame) with angular velocity $\boldsymbol{\omega}_B$ as shown in Fig. 3.5. The evolution of this vector in time can be written as follows:

$$\dot{\boldsymbol{n}} = -\boldsymbol{\omega}_B \times \boldsymbol{n} \tag{3.17}$$
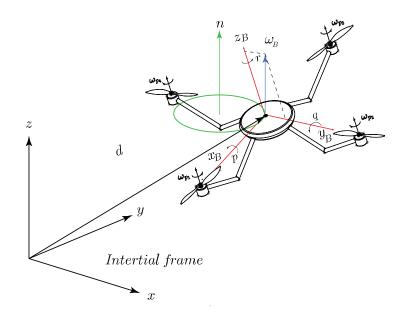
Fig. 3.5. Representation of the unit vector $\boldsymbol{n}$ in a quadcopter after the failure of motor number 4. The green circle represents the periodic motion of the quadcopter about $\boldsymbol{n}$. As it can be seen, $\boldsymbol{n}$ and $\boldsymbol{\omega}_B$ are parallel and they both are in parallel with the z-axis of the inertial frame.

According to the new hover definition, in hover, we want this unit vector to be fixed with respect to the vehicle. If $\boldsymbol{n}$ is fixed, (3.17) should be equal to zero. In other words, in hover, $\boldsymbol{n}$ is a unit vector stationary in the inertial frame as expressed in the body frame which is parallel to $\boldsymbol{\omega}_B$. Setting (3.17) to zero and knowing that $\boldsymbol{n}$ is a unit vector, one can write the followings (note that an overbar indicates equilibrium or hover values):

$$\dot{\boldsymbol{n}} = 0 \rightarrow \|\bar{\boldsymbol{n}}\| = \epsilon \|\bar{\boldsymbol{\omega}}_B\| \rightarrow \epsilon = \frac{1}{\|\bar{\boldsymbol{\omega}}_B\|} \tag{3.18}$$

Also, in hover, the projection of total thrust forces of all propellers onto $\bar{\boldsymbol{n}}$ should balance the weight of the vehicle which results in adding the following constraint to the system:

$$\sum_{i=1}^{4} \left(\boldsymbol{f}_{p_i} . \bar{\boldsymbol{n}} \right) = m\|\boldsymbol{g}\| \tag{3.19}$$

As the vehicle is turning with constant angular velocity $\bar{\boldsymbol{\omega}}_B$, the COM of the ith propeller goes through a rotation about $\bar{\boldsymbol{n}}$ which generates an almost uniform freestream velocity $\boldsymbol{V}_\infty = (0, 0, \bar{r}l)$ over the propeller as expressed in the body frame, where l is the distance of the COM of the propeller from the COM of the vehicle and $\bar{r}$ is the yaw rate of the vehicle in hover. Considering this freestream velocity vector, using the proposed propeller model and the resultant angular velocity of the airflow over the propellers, equations (2.2), (2.3) and (2.4) can be rewritten as follows:

$$df_p = \frac{1}{2}\rho_a c C_L \left(r_b \big(\|\boldsymbol{\omega}_{p_i}\| + \bar{r} \big) + \bar{r}l \sin \psi_{p_i} \right)^2 dr_b \tag{3.20}$$

$$d\tau_{d_p} = \frac{1}{2}\rho_a c C_D \left(r_b \big(\|\boldsymbol{\omega}_{p_i}\| + \bar{r} \big) + \bar{r}l \sin \psi_{p_i} \right)^2 r_b dr_b \tag{3.21}$$

$$d\tau_p = \frac{1}{2}\rho_a c C_L \left(r_b \big(\|\boldsymbol{\omega}_{p_i}\| + \bar{r} \big) + \bar{r}l \sin \psi_{p_i} \right)^2 r_b \sin \psi dr_b \tag{3.22}$$

By integrating the above equations over the blade radius and averaging for all azimuth angles, average total thrust force and moments of the ith propeller can be calculated as follows:

$$f_p = \rho_a c C_L \left(\frac{R_b^3 \|\boldsymbol{\omega}_p\|^2}{3} + \frac{R_b^3 \bar{r}^2}{3} + \frac{R_b \bar{r}^2 l^2}{2} + \frac{2R_b^2 \bar{r} \|\boldsymbol{\omega}_p\|}{3} \right) \tag{3.23}$$

$$\tau_{d_p} = \rho_a c C_D \left(\frac{R_b^4 \|\boldsymbol{\omega}_p\|^2}{4} + \frac{R_b^4 \bar{r}^2}{4} + \frac{R_b^2 \bar{r}^2 l^2}{2} + \frac{2R_b^4 \bar{r} \|\boldsymbol{\omega}_p\|}{2} \right) \tag{3.24}$$

$$\tau_p = \rho_a c C_L \left(\frac{R_b^3 \|\boldsymbol{\omega}_p\| \bar{r}l + R_b^3 \bar{r}^2 l}{3} \right) \tag{3.25}$$

Using equations (2.14) and (3.17)- (3.25), by setting angular accelerations to zero and considering the proposed propeller model, a system of eight algebraic equations for 11 unknowns are obtained. Three more equations are required to solve the system. The unknowns are: $\bar{p}$, $\bar{q}$, $\bar{r}$, $\bar{n}_x$, $\bar{n}_y$, $\bar{n}_z$, ϵ, $\|\bar{\boldsymbol{\omega}}_{p1}\|$, $\|\bar{\boldsymbol{\omega}}_{p2}\|$, $\|\bar{\boldsymbol{\omega}}_{p3}\|$, $\|\bar{\boldsymbol{\omega}}_{p4}\|$. Assuming that motor number 4 is failed ($\|\bar{\boldsymbol{\omega}}_{p4}\| = 0$) and by adding the following constraints we will end up with a system of 11 algebraic equations with 11 unknowns.

$$\|\bar{\boldsymbol{\omega}}_{p1}\| = \|\bar{\boldsymbol{\omega}}_{p3}\| \qquad \rho = \left(\frac{\|\bar{\boldsymbol{\omega}}_{p2}\|}{\|\bar{\boldsymbol{\omega}}_{p1}\|} \right)^2 \tag{3.26}$$

43

where ρ is a tuning factor and a non-negative real number. Now there are 11 algebraic equations to be solved for 11 unknowns to obtain equilibrium values or hover solution.

We assume $\mathbf{I}^p \ll \mathbf{I}^B$. Also, since yaw is the dominant rotational motion, $\boldsymbol{\tau}_{d_B}$ in (2.16) is assumed to oppose yaw motion only and is assumed to be proportional to yaw rate with coefficient λ as follows:

$$\boldsymbol{\tau}_{d_B} = (0, 0, -\lambda r)^T \tag{3.27}$$

Using the reaction moment of the propeller and its angular velocity, the mechacnial power of the propellers in hover can be calculated as follows:

$$\bar{P}_p = \bar{\tau}_{d_p} \|\bar{\boldsymbol{\omega}}_p\| \tag{3.28}$$

As an example, consider a vehicle of mass $m = 0.5$ kg, $I_{xx} = I_{yy} = 3.2 \times 10^{-3}$ kg.m^2, $I_{zz} = 5.5 \times 10^{-3}$ kg.m^2, $l = 0.17$ m, $I_{zz}^p = 1.5 \times 10^{-5}$ kg.m^2 and $\lambda = 2.75 \times 10^{-3}$ N.m.s/rad. The propellers have two blades with $c = 0.03$ m, $C_L = 1.022$, $R_b = 0.08$ m and air density is assumed to be constant $\rho_a = 1.225$ kg/m^3. Using (2.14), (3.17)-(3.25), (3.26)- (3.28) and by performing a line search over the tuning factor ρ in (3.26), the minimum-power hover solution can be found as follows:

$$\rho = 0.38, \ \bar{\boldsymbol{n}} = (0, 0.25, 0.97)^T, \ \bar{\boldsymbol{\omega}}_B = (0, 5.11, 19.57)^T \ \text{rad/s}$$

$$\|\bar{\boldsymbol{\omega}}_{p_1}\| = \|\bar{\boldsymbol{\omega}}_{p_3}\| = -584.7 \ \text{rad/s}, \ \ \|\bar{\boldsymbol{\omega}}_{p_2}\| = 360.4 \ \text{rad/s}, \ \ \|\bar{\boldsymbol{\omega}}_{p_4}\| = 0$$

$$\bar{\tau}_{p_1} = -\bar{\tau}_{p_3} = (0, 0.013, 0)^T \ \text{N.m}, \ \ \bar{\tau}_{p_2} = (0.008, 0, 0)^T \ \text{N.m} \qquad (3.29)$$

$$\bar{\tau}_{p_4} = 0, \ \ \bar{f}_{p_1} = \bar{f}_{p_3} = 2.06 \ \text{N}, \ \ \bar{f}_{p_2} = 0.94 \ \text{N}, \ \ \bar{f}_{p_4} = 0$$

$$\bar{P}_{hover} = \sum_{i=1}^{4} \bar{P}_{p_i} = 46.52 \ \text{W}$$

Having defined the equilibrium (hover) states of the vehicle after failure in motor number 4, we continue by presenting the control algorithm. A cascaded control strategy is used to control attitude and position of the vehicle. First, using nonlinear equations of rotational motion in (2.14), a linear time-invariant system is introduced to be used in controlling the attitude of the vehicle or in other words control the direction of the unit vector $\boldsymbol{n}$. Second, it is shown that by controlling two attitude degrees of freedom that are related to the translational motion (n_x and n_y), along with sum of all the thrust forces, position of the vehicle can be controlled as well.

In controlling the attitude, the strategy is to give up control of the full attitude after failure. Instead, only those attitude degrees of freedom related to translation motion of the vehicle will be controlled which is often called reduced attitude control [23]. After failure, reduced attitude states are represented by a variable $\boldsymbol{\zeta} = (p, q, n_x, n_y)$ which includes pitch and roll rates of the vehicle and x- and y-components of the unit vector $\boldsymbol{n}$. By linearizing (2.14) and (3.17) about the equi-

librium state $\bar{\boldsymbol{\zeta}} = (\bar{p}, \bar{q}, \bar{n}_x, \bar{n}_y)$, the deviations of $\boldsymbol{\zeta}$ from $\bar{\boldsymbol{\zeta}}$ represented by $\tilde{\boldsymbol{\zeta}}$ can be described by the following linear time-invariant system:

$$
\dot{\tilde{\boldsymbol{\zeta}}} = \mathbf{A}\tilde{\boldsymbol{\zeta}} + \mathbf{B}\boldsymbol{u}, \quad
\mathbf{A} = \left.\frac{\partial \dot{\tilde{\boldsymbol{\zeta}}}}{\partial \tilde{\boldsymbol{\zeta}}}\right|_{\tilde{\zeta}=\bar{\zeta}} =
\begin{bmatrix}
0 & a & 0 & 0 \\
-a & 0 & 0 & 0 \\
0 & -\bar{n}_z & 0 & \bar{r} \\
\bar{n}_z & 0 & -\bar{r} & 0
\end{bmatrix},
\quad
\mathbf{B} = \frac{l}{I_{xx}^B}
\begin{bmatrix}
0 & 1 \\
1 & 0 \\
0 & 0 \\
0 & 0
\end{bmatrix}
\tag{3.30}
$$

where a and $\boldsymbol{u}$ are as follows:

$$
\begin{aligned}
a &= \frac{I_{xx}^B - I_{zz}^B}{I_{xx}^B}\bar{r} - \frac{I_{zz}^P}{I_{xx}^B}(\|\bar{\boldsymbol{\omega}}_{p1} + \bar{\boldsymbol{\omega}}_{p2} + \bar{\boldsymbol{\omega}}_{p3} + \bar{\boldsymbol{\omega}}_{p4}\|) \\
u_1 &= (f_{p3} - \bar{f}_{p3}) - (f_{p1} - \bar{f}_{p1}) \\
u_2 &= (f_{p2} - \bar{f}_{p2})
\end{aligned}
\tag{3.31}
$$

Also, the remaining degree of freedom to balance the weight of the vehicle can be determined by the following constraint:

$$
f_{p1} + f_{p2} + f_{p3} = \bar{f}_{p1} + \bar{f}_{p2} + \bar{f}_{p3}
\tag{3.32}
$$

By designing a linear controller for (3.30), the inner loop of the cascaded controller is complete. In order to control the position of the vehicle, an outer control loop is designed such that it generates reference signal for the inner control loop. This can

be done first by finding the desired acceleration of the vehicle to get to the desired position and then transforming it to the desired direction of the unit vector $\boldsymbol{n}$.

To control the position of the vehicle, the desired acceleration can be found by defining a new state variable $\tilde{\boldsymbol{d}}$ as expressed in the inertial frame, as the deviations of the position of the vehicle $\boldsymbol{d}$ from its desired position $\boldsymbol{d}_d$, behaving like a second order system with damping ratio ξ and natural frequency ω_n as follows:

$$\ddot{\boldsymbol{d}}_d = -2\xi\omega_n\dot{\tilde{\boldsymbol{d}}} - \omega_n^2\tilde{\boldsymbol{d}} \tag{3.33}$$

We define the total acceleration of the vehicle to be $(\ddot{\boldsymbol{d}}_d - \boldsymbol{g})$ as expressed in the inertial frame. In hover, we want $\ddot{\boldsymbol{d}}_d = 0$ so that the desired direction of the unit vector $\boldsymbol{n}$ will be in the opposite direction of $\boldsymbol{g}$. According to the Newton's second law, (3.19) and (3.33) one can write the following equation:

$$\left(\sum_{i=1}^{4} \boldsymbol{f}_{p_i}.\bar{\boldsymbol{n}}\right)\boldsymbol{n}_d = m^I\mathbf{R}_{\mathbf{B}}^{\mathbf{T}}\left(\ddot{\boldsymbol{d}}_d - \boldsymbol{g}\right) \tag{3.34}$$

where $\boldsymbol{n}_d$ represents the desired direction of the unit vector $\boldsymbol{n}$ which also determines the desired direction of the average total thrust force vector of the quadcopter. Intuitively, it means that if the average total thrust force vector is in the direction of $\boldsymbol{n}_d$, position control can be achieved. Finally, $\boldsymbol{n}_d$ can be calculated from (3.34) as follows:

$$\boldsymbol{n}_d = \frac{m^I\mathbf{R}_{\mathbf{B}}^{\mathbf{T}}\left(\ddot{\boldsymbol{d}}_d - \boldsymbol{g}\right)}{\sum_{i=1}^{4}\boldsymbol{f}_{p_i}.\bar{\boldsymbol{n}}} \tag{3.35}$$

In summary, the outer control loop controls the position of the vehicle and generates reference signal for the inner control loop which controls the reduced attitude of the vehicle. Note that the inner loop should be faster than the outer loop due to having faster dynamics.

For the example vehicle in (3.29) and using the calculated hover solution a linear-quadratic regulator (LQR) is designed to stabilize the vehicle. For the LQR controller, diagonal cost matrices $\mathbf{R}$ and $\mathbf{Q}$ are chosen with cost values 1 on the angular rates and 50 on deviations from the x- and y-components of $\bar{\boldsymbol{n}}$. In the translational controller, damping ratio ξ and natural frequency ω_n are chosen to be 0.7 and 1 respectively for all translational degrees of freedom. From the parameters of the system used in (3.29), $\mathbf{A}$ and $\mathbf{B}$ matrices are calculated as follows:

$$
\mathbf{A} = \begin{bmatrix} 0 & -17.8534 & 0 & 0 \\ 17.8534 & 0 & 0 & 0 \\ 0 & -0.9700 & 0 & 19.57 \\ 0.9700 & 0 & -19.57 & \end{bmatrix}, \quad \mathbf{B} = \begin{bmatrix} 0 & 53.1250 \\ 53.1250 & 0 \\ 0 & 0 \\ 0 & 0 \end{bmatrix} \tag{3.36}
$$

Consequently, the LQR control gain can be calculated as follows:

$$
\mathbf{k}_{lqr} = \begin{bmatrix} -0.0152 & 0.5361 & -2.1448 & -1.5811 \\ 3.1632 & -0.0759 & -1.4141 & 1.5812 \end{bmatrix} \tag{3.37}
$$

Using (3.29), (3.36) and (3.37), the controller is implemented using the nonlinear equations of motion to stabilize the vehicle. Simulation results are presented in

Fig. 3.6. In the simulations, it is assumed the vehicle is hovering at its initial position $\boldsymbol{d}_0 = (0, 0, 10)$ m and all motors are working properly. Suddenly at $t_0 = 0$ motor number 4 is turned off and the controller in (3.37) stabilizes the vehicle. The desired position after failure is to be at $\boldsymbol{d}_d = (10, 0, 15)$ m.

From Fig. 3.6, it can be seen that the proposed simple control strategy does a good job in controlling the position and reduced attitude of the vehicle. The oscillations in the steady states are due the periodic nature of the newly defined hover condition. The results show that even after a failure, altitude control can still be achieved because in multi-rotor UAVs the motors are usually operating at around 50% duty cycle. Therefore, even after losing two rotors, the UAV will still be able to maintain its altitude. Also, variations of thrust force for all propellers are presented in Fig. 3.7 where they converge to their equilibrium values found in (3.29).

3.3 Flight Control of Spinning UAVs with Streamline-shape Fuselage

This section presents development of a control strategy for the spinning UAV proposed in Chapter 2. The strategy is very similar to that of a quadcopter with one rotor failure presented in the previous section. However, a few modifications are required as the number of rotors is reduced to two and the fuselage has become streamline-shape which generates extra lift in the system. First, we begin with finding the equilibrium states (hover solution) of the vehicle.
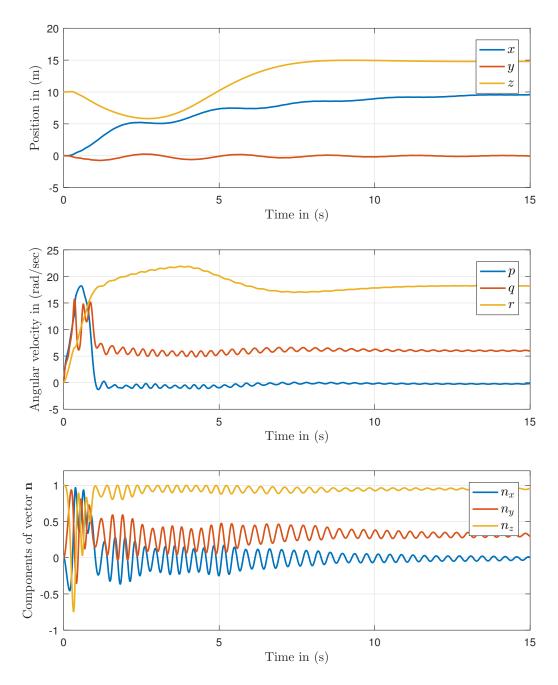
Fig. 3.6. Simulation results for stabilizing a quadcopter after one rotor failure. The position of the vehicle is controlled as well.

According to this new definition of hover, the vehicle must maintain an altitude while rotating with angular velocity $\boldsymbol{\omega}_B$ about the axis $\boldsymbol{n}$ that is fixed with respect to the vehicle and is expressed in the body frame. From (3.17) and (3.18) we have:
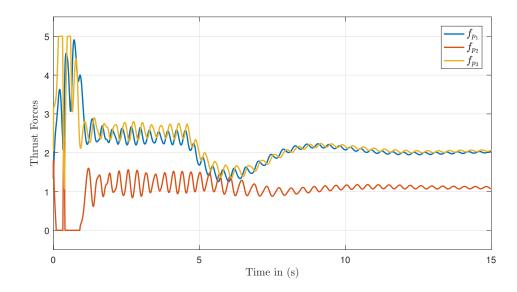
Fig. 3.7. Variations of thrust force for all propellers of the quadcopter after one rotor failure.

$$\dot{\boldsymbol{n}} = -\boldsymbol{\omega}_B \times \boldsymbol{n} \tag{3.38}$$

$$\dot{\boldsymbol{n}} = 0 \rightarrow \|\bar{\boldsymbol{n}}\| = \epsilon\|\bar{\boldsymbol{\omega}}_B\| \rightarrow \epsilon = \frac{1}{\|\bar{\boldsymbol{\omega}}_B\|} \tag{3.39}$$

where an overbar indicates the equilibrium (hover) condition.

Similar to the quadcopter with one rotor failure, this unit vector $\bar{\boldsymbol{n}}$ must be parallel to the gravitational acceleration vector $\boldsymbol{g}$ in order to maintain altitude. Therefore, the projection of average total thrust force, when the vehicle is spinning, onto the unit vector $\bar{\boldsymbol{n}}$ should be equal to the weight of the vehicle. In other words, the unit

51

vector $\boldsymbol{n}$ shows the direction of the average total acceleration of the vehicle. This can be written mathematically as follows:

$$\left(\bar{\boldsymbol{f}}_B + \sum_{i=1}^{4} \boldsymbol{f}_{p_i}\right).\bar{\boldsymbol{n}} = m\|\boldsymbol{g}\| \tag{3.40}$$

Using equations (2.18), (3.38)- (3.40) and by setting angular accelerations to zero, a system of seven algebraic equations for eight unknowns are obtained. One more equation is required to solve the system and to find the hover solution. The unknowns are: $\bar{p}$, $\bar{q}$, $\bar{r}$, $\bar{n}_x$, $\bar{n}_y$, $\bar{n}_z$, and $\|\bar{\boldsymbol{\omega}}_{p_1}\|$, $\|\bar{\boldsymbol{\omega}}_{p_2}\|$. Assuming $\|\bar{\boldsymbol{\omega}}_{p_1}\| = \|\bar{\boldsymbol{\omega}}_{p_2}\| = \|\bar{\boldsymbol{\omega}}_p\|$, in both monospinner and bispinner configurations, we add an additional constraint to the system. Therefore, eight algebraic equations can now be solved for eight unknowns to find the hover solution.

After finding the hover solution and using the proposed propeller model in presence of freestream velocity, total mechanical power in the system can be calculated as the sum of mechanical power of the propellers plus mechanical power of the streamline-shape fuselage as follows:

$$\bar{P} = \bar{P}_B + \sum_{i=1}^{3} \bar{P}_{p_i} = \|\bar{\boldsymbol{\tau}}_{d_B}\|\|\bar{r}| + \sum_{i=1}^{4} \left(\|\bar{\boldsymbol{\tau}}_{d_{p_i}}\|\|\bar{\boldsymbol{\omega}}_{p_i}\|\right) \tag{3.41}$$

Using (3.41), we will later define an objective function to determine optimal configurations for this spinning UAV.

The control structure is very similar to that of quadcopter with a rotor failure. First, from the nonlinear equations of motion a linear time-invariant system around

the hover solution is derived to describe the reduced attitude of the vehicle. Then, a linear time-invariant control strategy is developed to control the reduced attitude. By controlling the reduced attitude and altitude, it is shown that the direction of the unit vector $\boldsymbol{n}$ can be controlled. In the end, it is shown that by controlling x- and y-components of $\boldsymbol{n}$ (that are related to translation motion) and total acceleration of the vehicle, position control can be achieved as well.

The strategy is to give up control of full attitude degrees of freedom and instead, only the two attitude degrees of freedom related to translational motion will be controlled. Therefore, a new state variable, including pitch and roll rates of the vehicle and x- and y- components of the unit vector $\boldsymbol{n}$, as $\boldsymbol{\zeta} = (p, q, n_x, n_y)$ is defined to represent the reduced attitude of the vehicle. Furthermore, the deviations of $\boldsymbol{\zeta}$ from its equilibrium state $\bar{\boldsymbol{\zeta}} = (\bar{p}, \bar{q}, \bar{n}_x, \bar{n}_y)$ is written as $\tilde{\boldsymbol{\zeta}} = \boldsymbol{\zeta} - \bar{\boldsymbol{\zeta}}$ and its evolution as a first order system is as follows:

$$
\dot{\tilde{\boldsymbol{\zeta}}} = \mathbf{A}\tilde{\boldsymbol{\zeta}} + \mathbf{B}\boldsymbol{u}, \quad \mathbf{A} = \left.\frac{\partial \dot{\tilde{\boldsymbol{\zeta}}}}{\partial \tilde{\boldsymbol{\zeta}}}\right|_{\tilde{\boldsymbol{\zeta}}=\bar{\boldsymbol{\zeta}}} = \begin{bmatrix} 0 & a & 0 & 0 \\ -a & 0 & 0 & 0 \\ 0 & -\bar{n}_z & 0 & \bar{r} \\ \bar{n}_z & 0 & -\bar{r} & 0 \end{bmatrix}, \quad \mathbf{B} = \begin{bmatrix} b_1 \\ b_2 \\ 0 \\ 0 \end{bmatrix} \tag{3.42}
$$

where a, b_1 and b_2 are as follows:

$$a = \frac{I_{xx}^B - I_{zz}^B}{I_{xx}^B} \bar{r} - \frac{2I_{zz}^p \|\bar{\boldsymbol{\omega}}_p\| \cos \delta}{I_{xx}^B}$$

$$b_1 = \frac{l \cos \delta}{I_{xx}^B} - \frac{3C_{D_p} R_p \sin \delta}{4I_{xx}^B C_{L_p}} \qquad (3.43)$$

$$b_2 = \frac{h \sin \delta}{I_{xx}^B}$$

Although $\mathbf{A}$ and $\mathbf{B}$ matrices in (3.42) remain the same for both configurations, the control input for each configuration would be different. In monospinner configuration, the control input in (3.42) can be written as follows:

$$u_{monospinner} = (f_{p_1} - \bar{f}_{p_1}) + (f_{p_2} - \bar{f}_{p_2}) \qquad (3.44)$$

whereas in bispinner configuration, the control input is written as:

$$u_{bispinner} = (f_{p_1} - \bar{f}_{p_1}) - (f_{p_2} - \bar{f}_{p_2}) \qquad (3.45)$$

Using (3.42)- (3.45), x- and y- components of the unit vector $\boldsymbol{n}$ can be controlled. Intuitively, although only two moments about x- and z-axis (roll and yaw) could be manipulated directly, the moment about y-axis (pitch) could be manipulated indirectly using the cross-coupling of angular momentum in the system which enables us to control pitch and roll rates and thus the reduced attitude of the vehicle. Further-

more, an additional degree of freedom to balance the weight of the vehicle can be resolved by the following constraint:

$$f_{p_1} + f_{p_2} + f_B = \bar{f}_{p_1} + \bar{f}_{p_2} + \bar{f}_B \tag{3.46}$$

Similar to the quadcopter with one rotor failure, since $\boldsymbol{n}$ represents the direction of average total acceleration of the vehicle, one can control the position of vehicle by controlling the magnitude of total acceleration and the direction of $\boldsymbol{n}$. We can control the direction of $\boldsymbol{n}$ using the reduced attitude controller derived in (3.42)- (3.45). If we define the deviations of position of the vehicle $\boldsymbol{d}$ from its desired position $\boldsymbol{d}_d$ as $\tilde{\boldsymbol{d}}$, expressed in the inertial frame, to behave like a second order system with damping ratio ξ and natural frequency ω_n, then the acceleration vector can be found as follows:

$$\ddot{\boldsymbol{d}} = -2\xi\omega_n\dot{\tilde{\boldsymbol{d}}} - \omega_n^2\tilde{\boldsymbol{d}} \tag{3.47}$$

Also, we always have to compensate for gravitational acceleration $\boldsymbol{g}$ which adds another term to (3.47). Therefore, the total desired acceleration for position control is written as:

$$\ddot{\boldsymbol{d}}_d = \ddot{\boldsymbol{d}} - \boldsymbol{g} \tag{3.48}$$

Finally, similar to (3.34), the desired direction of the unit vector $\boldsymbol{n}$ can be found as follows:

$$\left(\left(\bar{\boldsymbol{f}}_B + \sum_{i=1}^{4} \boldsymbol{f}_{p_i} \right) . \bar{\boldsymbol{n}} \right) \boldsymbol{n}_d = m^I \mathbf{R}_{\mathbf{B}}^{\mathbf{T}} \left(\ddot{\boldsymbol{d}}_d - \boldsymbol{g} \right) \tag{3.49}$$

55

$$\boldsymbol{n}_d = \frac{m^I \mathbf{R}_\mathbf{B}^\mathbf{T} \left(\ddot{\boldsymbol{d}}_d - \boldsymbol{g} \right)}{\left(\bar{\boldsymbol{f}}_B + \sum_{i=1}^4 \boldsymbol{f}_{p_i} \right) . \bar{\boldsymbol{n}}} \tag{3.50}$$

Note that in the nested loop control structure, the position control should be done at slower rate than the reduced attitude control because of the faster dynamics in rotation than that in the translation. Therefore, damping ratio ξ and natural frequency ω_n in (3.47), should be selected carefully.

3.3.1 Monospinners Simulation Results

Suppose we have a spinning UAV with monospinner configuration with the following physical parameters:

$$c_p = 0.03 \text{ m}, \quad c_B = 0.03 \text{ m}, \quad R_p = 0.08 \text{ m}, \quad R_B = 0.08 \text{ m},$$

$$\delta = 0.0 \text{ rad}, \quad m = 0.1728 \text{ kg}, \quad l = 0.08 \text{ m}, \quad h = 0,$$

$$C_{D_p} = 0.1, \quad C_{D_B} = 0.1, \quad C_{L_p} = 1.5, \quad C_{L_B} = 1.5,$$

$$I_{zz}^p = 1.5360 \times 10^{-5} \text{ kg.m}^2, \quad \mathbf{I}^B = \mathrm{diag}([8.96 \times 10^{-5}, 8.96 \times 10^{-5}, 1.022 \times 10^{-4}]) \text{ kg.m}^2$$

Using equations (2.18), (3.38)- (3.40) and by setting angular accelerations to zero, hover solution can be found as follows:

$$\bar{\boldsymbol{n}} = (0, 0.02, 0.999)^T, \quad \bar{\boldsymbol{\omega}}_B = (0, 7.02, -300.19)^T \text{ rad/s}$$

$$\|\bar{\boldsymbol{\omega}}_{p_1}\| = \|\bar{\boldsymbol{\omega}}_{p_2}\| = 512.46 \text{ rad/s} \tag{3.51}$$

$$\bar{f}_{p_1} = \bar{f}_{p_2} = 0.424 \text{ N}, \quad \bar{f}_B = 0.848 \text{ N}$$

Using the calculated hover solution a linear-quadratic regulator (LQR) is designed to stabilize the vehicle. For the LQR controller, diagonal cost matrices $\mathbf{R}$ and $\mathbf{Q}$ are chosen with cost values 0 on the angular rates and 10 on deviations from the x- and y-components of $\boldsymbol{n}$. In the translational controller, damping ratio ξ and natural frequency ω_n are chosen to be 0.7 and 1 respectively for all translational degrees of freedom. Eventually, $\mathbf{A}$ and $\mathbf{B}$ matrices are calculated as follows:

$$\mathbf{A} = \begin{bmatrix} 0 & -75.4292 & 0 & 0 \\ 75.4292 & 0 & 0 & 0 \\ 0 & 0.999 & 0 & -300.19 \\ -0.999 & 0 & 300.19 & \end{bmatrix}, \quad \mathbf{B} = \begin{bmatrix} 625 \\ 0 \\ 0 \\ 0 \end{bmatrix} \tag{3.52}$$

Consequently, the LQR control gain can be calculated as follows:

$$\mathbf{k}_{lqr} = \begin{bmatrix} 0.0397 & 0.0017 & -4.4571, -0.3664 \end{bmatrix} \tag{3.53}$$

Using (3.42), (3.52) and (3.53), the controller is implemented using the nonlinear equations of motion to stabilize the vehicle. Simulation results are presented in Fig. 3.8. In the simulations, it is assumed the vehicle starts at its initial position

$\boldsymbol{d}_0 = (0, 0, 3)$ m. Note that the monospinner configuration is highly sensitive to the geometry of the vehicle, simply because it is highly under-actuated. Therefore, we assume the vehicle starts from a condition very close to the hover solution and then we introduce a step change in the position reference of the vehicle. The desired position is set to be at $\boldsymbol{d}_d = (3, 2, 5)$ m. Simulation results for position control are presented in Fig. 3.8-Fig. 3.10.
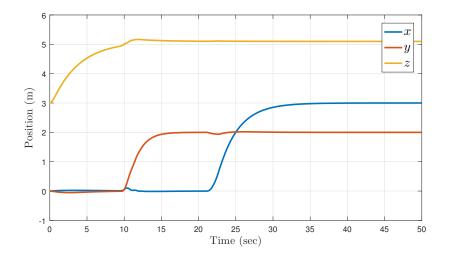
Fig. 3.8. Simulation results for stabilizing a monospinner. Results for position control from an initial position $\boldsymbol{d}_0$ to the desired position $\boldsymbol{d}_d$ are presented.

3.3.2 Bispinners

Now suppose we have a spinning UAV with bispinner configuration with the following physical parameters:

$$c_p = 0.03\text{m}, \quad c_B = 0.03 \text{ m}, \quad R_p = 0.08 \text{ m}, \quad R_B = 0.4 \text{ m},$$

58
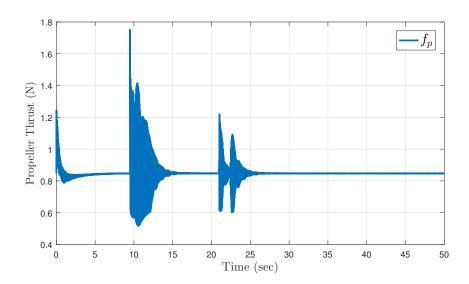
Fig. 3.9. Simulation results for stabilizing a monospinner. Variations of thrust force of the propeller is shown.
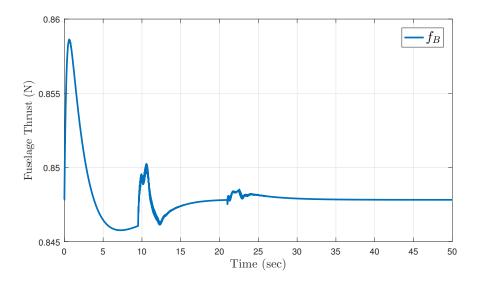
Fig. 3.10. Simulation results for stabilizing a monospinner. Variations of thrust force of the streamline-shape fuselage is shown.

$$\delta = 0.1 \text{ rad}, \quad m = 0.264 \text{ kg}, \quad l = 0.4 \text{ m}, \quad h = 0,$$

$$C_{D_p} = 0.1, \quad C_{D_B} = 0.1, \quad C_{L_p} = 1.5, \quad C_{L_B} = 1.5,$$

59

$$I_{zz}^p = 7.68 \times 10^{-5} \text{ m}, \quad \mathbf{I}^B = \text{diag}([9.6 \times 10^{-3}, 9.6 \times 10^{-3}, 1.92 \times 10^{-2}]) \text{ kg.m}^2,$$

Using equations (2.18), (3.38)- (3.40) and by setting angular accelerations to zero, hover solution can be found as follows:

$$\bar{\boldsymbol{n}} = (0,0,1)^T, \quad \bar{\boldsymbol{\omega}}_B = (0,0,-37.65)^T \text{ rad/s}$$

$$\|\bar{\boldsymbol{\omega}}_{p_1}\| = \|\bar{\boldsymbol{\omega}}_{p_2}\| = -184.54 \text{ rad/s} \tag{3.54}$$

$$\bar{f}_{p_1} = \bar{f}_{p_2} = 0.46 \text{ N}, \quad \bar{f}_B = 1.67 \text{ N}$$

Using the calculated hover solution a linear-quadratic regulator (LQR) is designed to stabilize the vehicle. For the LQR controller, diagonal cost matrices $\mathbf{R}$ and $\mathbf{Q}$ are chosen with all the diagonal elements being 1. In the translational controller, damping ratio ξ and natural frequency ω_n are chosen to be 0.7 and 1 respectively for all translational degrees of freedom. Eventually, $\mathbf{A}$ and $\mathbf{B}$ matrices are calculated as follows:

$$\mathbf{A} = \begin{bmatrix} 0 & 29 & 0 & 0 \\ -29 & 0 & 0 & 0 \\ 0 & 1 & 0 & -37.65 \\ -1 & 0 & 37.65 & \end{bmatrix}, \quad \mathbf{B} = \begin{bmatrix} 29.55 \\ 0 \\ 0 \\ 0 \end{bmatrix} \tag{3.55}$$

Consequently, the LQR control gain can be calculated as follows:

$$\mathbf{k}_{lqr} = \begin{bmatrix} 1.3587 & -0.3838 & -0.2122 & -1.3982 \end{bmatrix} \tag{3.56}$$

Using (3.42), (3.52) and (3.53), the controller is implemented using the nonlinear equations of motion to stabilize the vehicle. Simulation results are presented in Fig. 3.8. In the simulations, it is assumed the vehicle starts hovering at its initial position $d_0 = (0, 0, 10)$ m. Note that for bispinner, because we have full control over pitch/roll moments, it is easier to stabilize the vehicle and is less sensitive to geometry of the vehicle (compared to monospinner). The desired position is set to be at $d_d = (5, 0, 12)$ m. Simulation results for position control are presented in Fig. 3.11 and Fig. 3.12. From the figures, it can be seen that the control performance is relatively better in bispinner than that in monospinner. It is simply because in bispinner configuration, at least one rotational degree of freedom (roll or pitch) can be controlled independently.
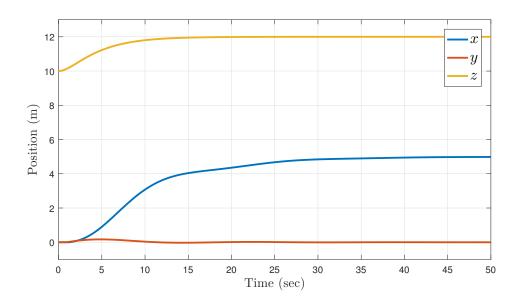

Fig. 3.11. Simulation results for stabilizing a bispinner. Results for position control from an initial position d_0 to the desired position d_d are presented.
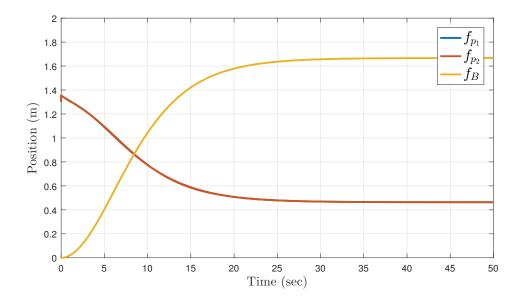
Fig. 3.12. Simulation results for stabilizing a bispinner. Variations of thrust forces generated by the propellers and the fuselage. Note that f_{p_1} and f_{p_2} are very close and fall on top of each other in this graph.

4

Performance Optimization

This chapter presents performance optimization for mutli-rotor UAVs. We start with investigating the effects of dihedral and twist angles on stability and maneuverability in quadcopters. These angles are introduced in Section 2.2. The results of this investigation will help to analytically identify quadcopter configurations with highest stability or maneuverability for the first time. Also, it could help to design reconfigurable vehicles which change shape, depending on flight conditions, to achieve some objectives according to mission requirements. In addition, by adding twist angle to quadcopters, a specific configuration could be found which not only yields to the minimum-power hovering in case of a rotor failure but also increases the stability of the vehicle in absence of an actuator failure.

We continue by investigating the performance of spinning-type UAVs. In particular, we define an optimization problem to find the optimal configurations in monospin-

ners and bispinners which results in not only having the minimum power consumption in hover, but also having the best trajectory tracking performance. In finding these configurations, we take into account the effects of nonzero freestream, the proposed propeller model and the complete nonlinear models presented in Chapter 2. Finally, optimal configurations for each type of UAVs is presented and design guidelines are provided.

4.1 Optimal Design in Quadcopters

The focus of this section is on quadcopters. We start with introducing the dihedral and twist angles to the vehicle and presenting their effects on stability of the vehicle analytically. We present six different configurations ranking from the most stable to the most maneuverable. Later, we show that one of these configurations yields the optimal-power hover solution in quadcopters in case of a rotor failure. The results are validated using numerical analysis.

4.1.1 Optimal design for stability

In this section, an aerodynamic phenomenon, called dihedral effect, which is very common in fixed-wing aircrafts is introduced [37]. Suppose we have a quadcopter as shown in Fig 4.1 and each rotor can be tilted independently about x- and y-axis of its corresponding frame M_i. From Section 2.2, the tilting angle about x-axis is called

twist angle α_i and the tilting angle about the y-axis is called dihedral angle β_i. The positive direction of rotation can also be found in Section 2.2.
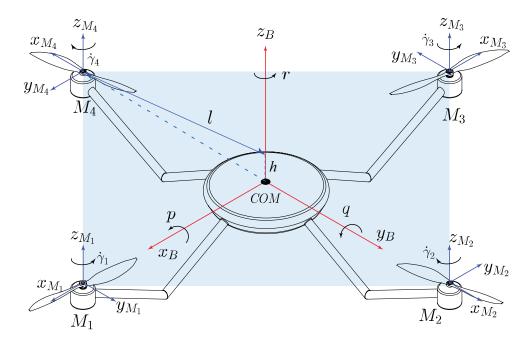
Fig. 4.1. Quadcopter in "+" configuration. Body frame is shown in blue and is attached to the center-of-mass of the quadcopter. A frame, shown in blue, is attached to each motor in order to determine orientation of the motors with respect to body frame. Motors are located at distance l and h from z-axis and x-y plane of the body frame respectively.

Furthermore, in Section 2.1, by introducing the effects of having nonzero freestream velocity on propeller's performance, we concluded that "any freestream with positive (negative) z-component velocity, as expressed in the propeller's frame M_i, increases (decreases) the AOA which increases (decreases) the thrust force".

Now consider a quadcopter in 2D motion. In Fig 4.2, a configuration with no twist angle ($\alpha_i = 0$) and constant dihedral angle $\beta_i = b$ (b is negative) is shown. Suppose the vehicle is pitching down and moving to the left which is equivalent of having an

air flow with horizontal velocity to the right as shown in blue color in the figure. According to "Dihedral Effect", for the left motor, there will be an airflow with positive z-component in the corresponding frame M_i as shown in green color, and similarly, for the right motor, there will be an airflow with negative z-component velocity in the corresponding frame M_i. As a result, the AOA in the left rotor increases thus its thrust force increases. However for the right rotor, the AOA decreases and thrust force decreases as well. This interesting effect can make the vehicle stable in translational motion. As the vehicle moves to the left, due to the difference between thrust force of the left and right motors, a moment q', is generated that acts like damping in the system which resists with pitching and attempts to bring pitch angle to zero.
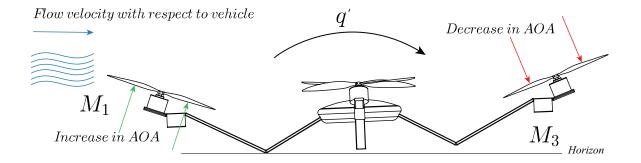
Fig. 4.2. Dihedral effect in 2D motion of a quadcopter. The quadcopter is pitching down and moving to the left. Dihedral effect generates the moment q' and acts like damping in the system.

From (2.10), one can derive an equation to determine the changes in thrust force of the propellers as follows:

$$\|^{M_i}\Delta\boldsymbol{f}_{p_i}\| = \frac{1}{4}\rho_a c\sigma R_b^2\|\boldsymbol{V}_\infty\||\dot{\gamma}_i| \tag{4.1}$$

where $\dot{\gamma}_i$ is the angular velocity of the ith propeller about z-axis of frame M_i and $\boldsymbol{V}_\infty$ is the freestream velocity vector which is in the direction of z-axis of the frame M_i.

Near hover condition, if we consider $\dot{\gamma}_i$ to be constant then (4.1) can be simplified further as follows:

$$\|^{M_i}\Delta\boldsymbol{f}_{p_i}\| = -\zeta\|\boldsymbol{V}_\infty\|, \quad \zeta = \frac{1}{4}\rho_a c\sigma R_b^2|\dot{\gamma}_i| \tag{4.2}$$

We call equation (4.2) the "Pitch Damper" and likewise, one can derive an equation for "Roll Damper". The reason we call this a damper is because any pitching moment generates a freestream over the propellers which changes their thrust force according to (4.2), and this change in thrust force generates a moment counteracting that original pitching moment.

Effects of twist angle α_i also falls in the category of "Dihedral Effects". As shown in Fig 4.3, to damp yaw motion, we need to choose $\alpha_{1,3} > 0$ and $\alpha_{2,4} < 0$. This is an interesting case where dihedral effect damps yaw motion. To better visualize this effect, assume that the quadcopter has a positive rotation about axis z_B. In this case, due to dihedral effect, AOA of propellers 2 and 4 decreases since there is an airflow with negative z-component of its linear velocity in the corresponding frames

67

$M_{2,4}$. On the other hand, there will be an air flow with positive z-component of its linear velocity in the corresponding frames $M_{1,3}$. This phenomenon, generates a yaw moment (shown in green) that resists yaw motion r. Note that using $\alpha_{1,3} < 0$ and $\alpha_{2,4} > 0$ will have an adverse effect on yaw motion and could make the vehicle unstable.
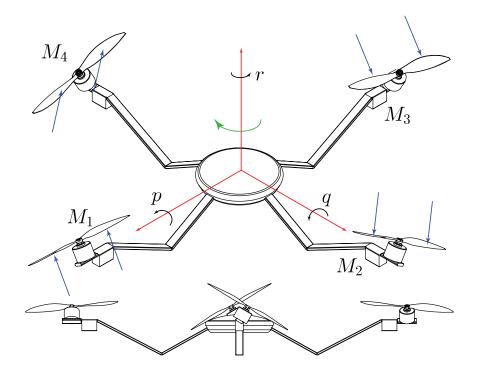
Fig. 4.3. Quadcopter having only twist angles $\alpha_{1,3} > 0$ and $\alpha_{2,4} < 0$. The vehicle is going through pure yaw motion r and dihedral effect generates a counteracting yaw motion.

In summary, these changes in thrust force of the propellers generate counteracting moments in all rotational degrees of freedom. These moments could affect overall stability of the vehicle. We continue by presenting stability analysis in yaw motion (roll and pitch will be similar).

For simplicity suppose $\beta_i = 0$, $\alpha_{1,3} > 0$ and $\alpha_{2,4} < 0$. Also, all of these angles are assumed to remain constant throughout the analysis. We assume, d is positive meaning that the center of mass is located below the flat plane in Fig 4.1. Using (2.14) and (2.16), the equations governing the rotational motion can be rewritten as follows:

$$\boldsymbol{\tau} = \begin{bmatrix} I_{xx}\dot{p} \\ I_{yy}\dot{q} \\ I_{zz}\dot{r} \end{bmatrix} + \begin{bmatrix} (I_{zz} - I_{yy})qr \\ (I_{xx} - I_{zz})pr \\ 0 \end{bmatrix} \tag{4.3}$$

where

$$\boldsymbol{\tau} = \begin{bmatrix} k_f h s_\alpha(\dot{\gamma_1}^2 - \dot{\gamma_3}^2) + (k_f l c_\alpha + k_t k_f s_\alpha)(\dot{\gamma_2}^2 - \dot{\gamma_4}^2) \\ k_f l c_\alpha(\dot{\gamma_4}^2 - \dot{\gamma_2}^2) + (k_t k_f s_\alpha + k_f h s_\alpha)(\dot{\gamma_3}^2 - \dot{\gamma_1}^2) \\ (k_t k_f c_\alpha - k_f l s_\alpha)(\dot{\gamma_1}^2 - \dot{\gamma_2}^2 + \dot{\gamma_3}^2 - \dot{\gamma_4}^2) \end{bmatrix} \tag{4.4}$$

Note that τ is the external torque generated by the rotors to control the attitude of the vehicle and $\dot{\gamma}_i$ is the angular velocity of the rotors. Also, s and c represent sine and cosine functions. It can be shown that $\alpha_i = 0$ yields equations of motion for a regular quadcopter without tilting angles. From (4.3) and (4.4), in a pure yaw motion, we have the following equation:

$$\tau_{yaw} = I_{zz}\dot{r} \tag{4.5}$$

69

From (4.4) and assuming the motors input for yaw motion to be equal to $u = \dot{\gamma_1}^2 - \dot{\gamma_2}^2 + \dot{\gamma_3}^2 - \dot{\gamma_4}^2$, we can rewrite (4.5) as follows:

$$\dot{r} = \frac{(k_t k_f c_\alpha - k_f L s_\alpha)}{I_{zz}} u \tag{4.6}$$

Taking Laplace transform of (4.6), we can derive yaw motion transfer function as follows:

$$\frac{r(s)}{u(s)} = \frac{C_1}{s} \tag{4.7}$$

where $C_1 = \frac{(k_t k_f c_\alpha - k_f L s_\alpha)}{I_{zz}}$.

Using (4.2), we can add the effects of twist angle into (4.6). Let's suppose the vehicle is going through pure yaw motion, r, as shown in Fig 4.2. This yaw motion will generate an almost uniform local airflow over each blade with linear velocity expressed in the body frame as follows:

$$^B\mathbf{v}_{p_i} = [0, 0, r]^T \times {}^B\mathbf{O}_{M_i} = [0, 0, (-1)^{i+1} r l s_{\alpha_i}]^T \tag{4.8}$$

where $^B\mathbf{O}_{M_i}$ is the position vector of COM of the ith propeller expressed in the body frame and l is the distance of the COM of the propeller to the COM of the vehicle. Using (4.2) and (4.8), we can write down the equation for changes in thrust force of each propeller expressed in the body frame as follows:

$$^B\Delta\mathbf{F}_{p_i,twist} = [0, 0, (-1)^{i+1} \zeta_{yaw} r l s_{\alpha_i}]^T \tag{4.9}$$

70

From (4.9) and considering all the changes in thrust force for all propellers, we can calculate the net moments due to twist angle α_i as follows:

$$\boldsymbol{\tau}_{twist} = \sum_{i=0}^{4} {}^B\mathbf{O}_{M_i} \times {}^B\Delta\mathbf{F}_{p_i,twist} \tag{4.10}$$

As shown in Fig 4.2, any yaw motion r, will generate an airflow with negative z-component of its linear velocity in the frames $M_{2,4}$. Likewise, it will generate an airflow with positive z-component of its linear velocity in the frames $M_{1,3}$. As a result, based on (4.10), a torque will be generated counteracting the yaw motion r. Considering the simplifying assumptions made earlier in this section, (4.10) can be rewritten as follows:

$$\boldsymbol{\tau}_{twist} = [0, 0, -4\zeta_{yaw} r l^2 s_{\alpha_i}^2]^T \tag{4.11}$$

Now, using (4.5) and the third component of (4.11), we can add the effects of twist angle as follows:

$$\tau_{yaw} + \tau_{twist} = I_{zz}\dot{r} \tag{4.12}$$

$$C_1 u = \dot{r} + \frac{\zeta'_{yaw}}{I_{zz}}r \tag{4.13}$$

where $\zeta'_{yaw} = 4\zeta_{yaw}L^2 s_a^2 > 0$. Finally, taking Laplace transform of (4.13) and simplifying will result in the following transfer function:

$$\frac{r(s)}{u(s)} = \frac{C_1}{s + \frac{\zeta'_{yaw}}{I_{zz}}} \tag{4.14}$$

Comparing (4.14) with (4.7), shows that the vehicle has become more stable indeed. Transfer function in (4.14) shows that it only has one negative pole indicating asymptotic stability in yaw motion. In addition to stability, this configuration helps to yaw faster because of the twist angle. Using twist angle, a component of thrust force can be used to generate yaw motion which can be larger and easier to generate compared to regular quadcopters which yaw using reaction moments of the rotors. Note that $\alpha_{1,3} < 0$ and $\alpha_{2,4} > 0$ will have adverse effect on stability and will destabilize the system or in other words, increases maneuverability.

Similarly, it can be shown that such phenomenon exists in roll and pitch motion for negative values of dihedral angle β_i and similar transfer functions can be derived. The effect of location of center of mass is hidden in the value of ζ' in roll and pitch motion. It can be shown that for $d > 0$, as d increases, the location of the pole of the transfer function will move to the left in the complex plane and increases stability and decreases maneuverability. Similarly, as d decreases (even for negative values), the location of the pole of the transfer function will move to the right in the complex plane and stability will be decreased and maneuverability will be increased.

As a corollary, based on dihedral and twist angles, six different configurations are proposed followed by a comparison in terms of stability and maneuverability. A regular quadcopter with all rotors' angles set to zero is considered as a reference for comparison. The sign of dihedral and twist angles for each rotor determines degree of stability or maneuverability in each configuration. The following list, ranks these

configurations from the most stable to the most maneuverable (for simplicity, we assume that d is positive for all configurations):

1. $\beta_i < 0$, $\alpha_{1,3} > 0$ and $\alpha_{2,4} < 0$

2. $\beta_i < 0$, $\alpha_i = 0$

3. $\beta_i = 0$, $\alpha_{1,3} > 0$ and $\alpha_{2,4} < 0$

4. $\beta_i = 0$, $\alpha_i = 0$ (flat configuration)

5. $\beta_i = 0$, $\alpha_{1,3} < 0$ and $\alpha_{2,4} > 0$

6. $\beta_i > 0$, $\alpha_{1,3} < 0$ and $\alpha_{2,4} > 0$

In configuration (1), dihedral and twist angles are in favor of the stability and three dampers for roll, pitch and yaw motion are active in the quadcopter and are helping to stabilize its rotational motion. In configuration (2), twist angles are all set to zero, meaning that no damping (due to twist angles) exist in yaw motion and only roll and pitch dampers are active which results in having a vehicle less stable compared to configuration (1). In Configuration (3), only yaw damper is active and in configuration (4) all dihedral and twist angles are set to zero representing a regular quadcopter without tilting angles of the motors. In configuration (5), twist angles have an adverse effect compared to what we had in configuration (1), meaning that twist angles in this configuration will destabilize yaw motion of the quadcopter.

Note that having an adverse effect on stability means that the poles of the transfer function will move rightward in the complex plane and in some cases the poles will

possibly fall in the right half of complex plane. Finally, in configuration (6), all dihedral and twist angles are having adverse effect with regard to stability in the system. However, in configurations (5) and (6), the vehicle has the highest maneuverability compared to other configurations.

In summary, depending on applications and the environment in which the quadcopter is operating, choosing the best configuration and optimized values for dihedral and twist angles will be a trade off between stability and maneuverability.

4.1.2 Optimal design for fault tolerant control

In this section, we investigate about the optimality of the configuration and hover solution, in a quadcopter after a rotor failure, in terms of power consumption. After failure, it is shown that at equilibrium, the vehicle will have constant angular velocity with yaw being the dominant rotational motion. In hover, according to (3.23)- (3.25), $\bar{r}$ can have significant effects on thrust force and the moment generated by the propellers depending on its magnitude and direction which consequently affects power consumption of the motors. In particular, a specific configuration can be introduced that generates $\bar{r}$ such that it is in favor of thrust force and the moment of the propeller and thus yielding the minimum-power hover solution.

In hover, $\bar{r}$ can affect the resultant angular velocity of the propeller and also can change the relative air flow velocity over the blade. In a quadcopter, because half of the rotors are turning in the opposite direction of the remaining half of the rotors, therefore after failure, $\bar{r}$ will have positive effect on some rotors and negative effect on

some other rotors. If the direction of $\bar{r}$ is the same (opposite) as that of the propeller's angular velocity, then the propeller should turn slower (faster) in order to generate the same amount of thrust force when $\bar{r} = 0$, therefore according to (3.24), (3.23) and (3.28), since $\bar{f}_{p_i}$ experiences very small changes (only for small angles), the power consumption of the motor will be decreased (increased). The goal of this section is to find the best configuration of the motors to get the most benefits out of $\bar{r}$ after failure, such that the power consumption of the motors is minimum.

In regular quadcopters, yaw motion is usually carried out using reaction moments of the propellers. This moment is fairly small compared to the moment generated by the propeller's thrust force about the center of mass of the vehicle [6], therefore it may not be an efficient way to yaw. Instead, one can yaw by tilting the rotors (the twist angle α_i presented in Section 2.2 in Fig 2.7) and using a small component of the propeller's thrust force to generate relatively larger yaw moments [12]. Note that the tilting angle should be small enough so that the component of the thrust force that balances the weight of the vehicle experiences small changes. Also, it has to be small enough such that the linear time-invariant fault-tolerant controller can stabilize the vehicle after the failure of one rotor. Therefore, using numerical simulations in Section 3.2 and to ensure stability after the failure, we assume $-0.4 \leq \alpha_i \leq 0.4$ rad.

A new configuration is proposed by tilting the rotors about the x-axis of each motor frame M_i as shown in Fig 4.4 where the positive direction of the tilting angle is shown in Fig 4.5. Because rotors 1 and 3 are assumed to be turning in the negative direction of z-axis of the body frame, by tilting these rotors by any positive angle,

the vehicle tends to generate a yaw motion that is in favor of reducing their power consumption. Whereas for rotors 2 and 4 which are turning in the positive direction of the z-axis of the body frame, the tilting angle should be negative. Note that it is assumed $\alpha_1 = \alpha_3$ and $\alpha_2 = \alpha_4$. The resulting configuration is presented in Fig 4.6. This new configuration not only helps to reduce the power consumption after failure, but also helps to increase stability of the vehicle in yaw motion in absence of failures [12]. It also adds a new tuning parameter α_i to the hover solution.
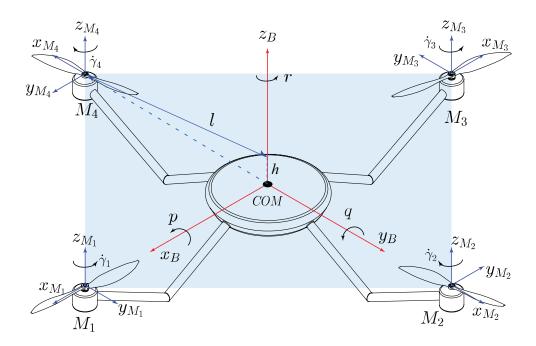
Fig. 4.4. A Quadcopter in "+" configuration. Motor frames and body frame are presented in blue and red respectively. Direction of rotation of propellers are presented as well.

Using equations (2.14) and (3.17)- (3.25), adding the effect of tilting angle, setting angular accelerations to zero, adding the constraints in (3.26), assuming that motor number 4 is failed ($\|\bar{\boldsymbol{\omega}}_{p_4}\| = 0$) and considering the proposed propeller model, a system
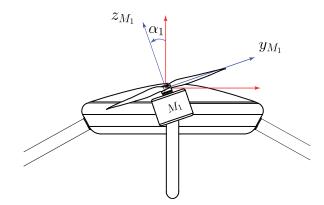
Fig. 4.5. Twist angle α_1 about the x-axis of the motor frame M_1.
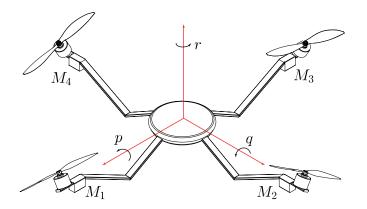
Fig. 4.6. The proposed configuration for quadcopter by introducing twist angle to the rotors.

of 11 algebraic equations for 11 unknowns are obtained. The system of algebraic equations can be solved numerically to obtain the hover solution. In this system of equations, there are two tuning parameters namely ρ and $|\alpha_i|$.

In order to find the minimum-power hover solution, a simple line search is performed over tuning parameters ρ and α_i. Results show that the minimum-power hover solution can be found when $\rho = 0$ and $\alpha_{1,3} = 0.4$ radians, meaning that after failure, motor number 2 should be turned off and rotors number 1 and 3 should be

tilted by 0.4 radians. For $\rho = 0$, Fig 4.7 shows the equilibrium value of total power consumption of the motors for all values of tilting angle $-0.4 \leq \alpha_i \leq 0.4$, Fig 4.8 shows the absolute value of yaw rate $\bar{r}$ at equilibrium for all values of α_i and Fig 4.9 shows the equilibrium value of angular velocity of the propellers with respect to the body frame for all values of α_i (note that $\bar{\boldsymbol{\omega}}_{p_1} = \bar{\boldsymbol{\omega}}_{p_3}$).
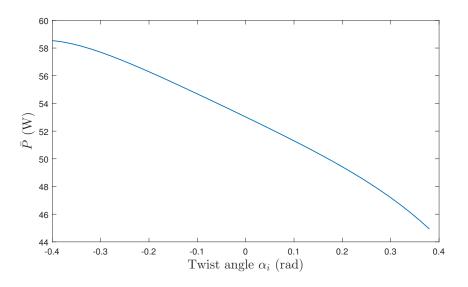
Fig. 4.7. Equilibrium value of total power consumption of the motors for all values of twist angle. Note that $\rho = 0$

From Fig 4.7, it can be seen that the minimum-power hover solution can be found when $\alpha_{1,3} = 0.4$ rad. Note that when tilting angle is zero and $\rho = 0$, $\bar{P}$ is almost 54 W which is larger than $\bar{P}$ in (3.29), meaning that having three motors on, actually consumes less power than having only two motors on (when $\alpha_i = 0$). However, after adding the effects of tilting the motors, it is shown that with only two motors one can find a hover solution with even less power consumption than with three motors.
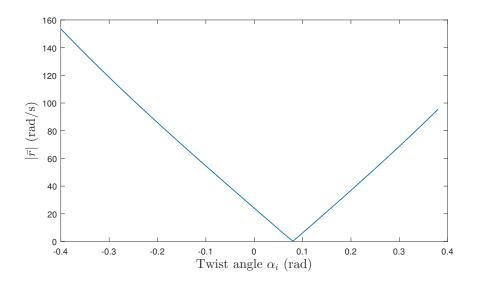
Fig. 4.8. The absolute value of yaw rate r at equilibrium for all values of twist angle. Note that $\rho = 0$
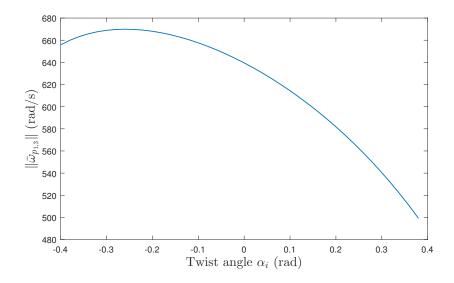
Fig. 4.9. The absolute value of angular velocity of the propellers at equilibrium with respect to the body frame for all values of twist angle. Note that $\rho = 0$

In Fig 4.8, despite having large yaw rates (absolute value) when α_i is negative, the power consumption is high, simply because the yaw motion is in the opposite direction

of the angular velocity of the propellers and it decreases the resultant airflow velocity over the blades. Therefore, the propellers must turn faster to balance the weight of the vehicle and as a result, the power consumption increases. As α_i approaches 0.08 radians, the absolute value of yaw rate approaches zero at equilibrium. Not that when $\bar{r} = 0$, according to (3.30), the system becomes uncontrollable. Furthermore, as α_i is greater than 0.08 and increasing, the absolute value of yaw rate starts increasing in favor of decreasing the power consumption of the motors.

Finally, in Fig 4.9, as α_i increases from -0.4 radians up to -0.26 radians, the absolute value of angular velocity of the propeller with respect to the body frame increases which is due to the interaction between the freestream velocity and the local airflow velocity over the blades. For all values of $\alpha_i \geq -0.26$, angular velocity of the propeller decreases up to its minimum value occurring at $\alpha_i = 0.4$ radians.

The minimum-power hover solution considering both tuning parameters ρ and $\alpha_{1,3} = 0.4$ can be found as follows:

$$\rho = 0.0, \quad \alpha_{1,3} = 0.4 \text{ rad}, \quad \bar{\boldsymbol{n}} = (0, 0, 1)^T,$$

$$\bar{\boldsymbol{\omega}}_B = (0, 0, -95.47)^T \text{ rad/s}$$

$$\|\bar{\boldsymbol{\omega}}_{p_1}\| = \|\bar{\boldsymbol{\omega}}_{p_3}\| = 499.2 \text{ rad/s}, \quad \|\bar{\boldsymbol{\omega}}_{p_2}\| = \|\bar{\boldsymbol{\omega}}_{p_4}\| = 0 \text{ rad/s},$$

$$\bar{\tau}_{p_1} = -\bar{\tau}_{p_3} = (0, -0.04, 0)^T \text{ N.m}, \quad \bar{\tau}_{p_2} = \bar{\tau}_{p_4} = 0$$

$$\bar{f}_{p_1} = \bar{f}_{p_3} = 2.06 \text{ N}, \quad \bar{f}_{p_2} = \bar{f}_{p_4} = 0$$

$$\bar{P}_{hover} = \sum_{i=1}^{4} \bar{P}_{p_i} = 44.9 \text{ W}$$

$$(4.15)$$

It is worth mentioning that controller performance in trajectory tracking can be added as an additional constraint to the system to find the optimal-power hover solution which not only yields a configuration with minimum power consumption in hover, but also has the best tracking performance. However, it can be shown through simulations that the performance of a nominal controller for the quadcopter with one or two rotor failures does not change much. Therefore, controller performance is assumed to be almost invariant to different configurations.

4.2 Optimal Design in Spinning UAVs

This section presents optimal hover solutions for the two configurations in spinning UAVs namely *Monospinners* and *Bispinners*. These solutions are not only optimal in terms of power consumption, but also are optimal in tracking a trajectory. We begin with defining a set of design variables and an objective function to minimize power consumption in hover while having the best performance in tracking a trajectory. In the end, extensive numerical analyses are carried out and design guidelines are provided.

We define a set of seven design variables as follows:

$$x = \left(\theta_p, \theta_B, \frac{c_B}{c_p}, \frac{R_B}{R_p}, \frac{l}{R_B}, \frac{h}{R_B}, \delta \right) \tag{4.16}$$

where θ_p and θ_B are pitch angles (in degrees) of the blades of propeller and fuselage respectively, $\frac{c_B}{c_p}$ is the ratio of fuselage's chord to propeller's chord, $\frac{R_B}{R_p}$ is the ratio

of fuselage's blade radius to propeller's blade radius, $\frac{l}{R_B}$ is the ratio of the distance

of COM of the propeller from COM of the vehicle to the fuselages blade radius, $\frac{h}{R_B}$

is the height of the COM of the propellers in the body from to the fuselage's blade

radius and δ is the tilting angle of the rotors in radian. Note that any configuration

can be described using (4.16).

In order to compare different configurations in terms of power consumption in

hover, specific power (power-to-weight ratio) is defined as a function of (4.16) as

follows:

$$P_s = \frac{\bar{P}}{m\|\boldsymbol{g}\|} = F(x) \qquad (4.17)$$

Note that equations of motion are highly nonlinear and the system of equations

used to find hover solution does not have an explicit solution. Therefore, they should

be solved numerically and for that we choose the following physical parameters of the

system:

$$c_p = 0.03 \text{ m}, \;\; R_p = 0.08 \text{ m}, \;\; \|\boldsymbol{g}\| = 9.81 \text{ m/s}^2, \;\; \rho_a = 1.225 \text{kg/m}^3 \qquad (4.18)$$

Also note, for each configuration, as $\frac{c_B}{c_p}$ and $\frac{R_B}{R_p}$ change, the total mass and moment

of inertia matrix of the vehicle will change accordingly.

Since the system is highly under-actuated, it is important to investigate about the

performance of the controller in tracking a trajectory. Therefore, to check tracking

performance, first, using (3.30) a nominal LQR controller with the following weight matrices is defined:

$$\mathbf{Q} = \text{diag}([1, 1, 10, 10]), \quad \mathbf{R} = 1 \tag{4.19}$$

where $\mathbf{Q}$ is the weight matrix for the states and $\mathbf{R}$ is the weight matrix for the control input. In (4.19), higher weights are given to the x and y components of $\boldsymbol{n}_d$. Furthermore, natural frequency and damping ratio of the position controller in (3.33) are set to 1. Using this nominal controller an objective as a function of percentage overshoot and steady state error, for all translational degrees of freedom, in response to a step change is defined as follows:

$$y = (PO_x, PO_y, PO_z, SS_x, SS_y, SS_z)$$
$$G(y) = a_1 PO_x^2 + a_2 PO_y^2 + a_3 PO_z^2 + a_4 SS_x^2 + a_5 SS_y^2 + a_6 SS_z^2 \tag{4.20}$$

where PO and SS represent percentage overshoot and steady state error respectively and a_i is a real number representing the weight given to each element of y in the cost function G(y).

Finally, the optimal configuration with minimum power consumption in hover having the best trajectory tracking performance can be found by defining a cost function by combining (28) and (33) as follows:

$$H(x, y) = b_1 F(x) + b_2 G(x) \tag{4.21}$$

where b_1 and b_2 are the weights given to power consumption of the vehicle and its trajectory tracking performance respectively.

Using (4.16) and (4.17), an optimization problem is defined to find the optimal configuration as follows:

$$\underset{x}{\text{argmin}} \quad H(x)$$

$$\text{subject to} \quad \text{equations of motion}$$

(4.22)

4.2.1 Monospinners

In this section, optimal solutions for hovering and trajectory tracking of monospinners are presented. We begin with configurations where the tilting angle is zero and in the end we discuss the results when taking the tilting angle into account. First using (4.16)- (4.21) and using simple blind search algorithm, we investigate about finding the best x which results in the minimum P_s.

Fig 4.10, shows the contours of P_s for variations of θ_p and θ_B. The results suggest that the optimal-power configuration can be achieved when having the maximum allowed pitch angle for both propeller and fuselage.

Next, by selecting the best values for θ_p and θ_B, we present the power consumption of hover solutions for variations of c_B/c_p and R_B/R_p . Using (4.17), contours of P_s versus variations of c_B/c_p and R_B/R_p can be drawn as shown in Fig 4.11.

Fig 4.11 shows that the optimal configuration can be achieved at the maximum allowed c_B/c_p and $R_B/R_p = 0.7$. This indicates that as R_B/R_p increases, P_s increases
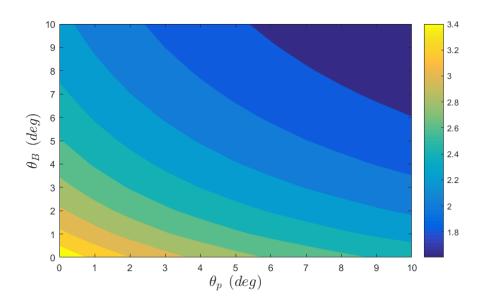
Fig. 4.10. Contours of P_s versus variations of θ_p and θ_B. In these simulations, $l/R_B = 1$, $h/R_B = 0.2$, $c_B/c_p = 1$ and $R_B/R_p = 2$
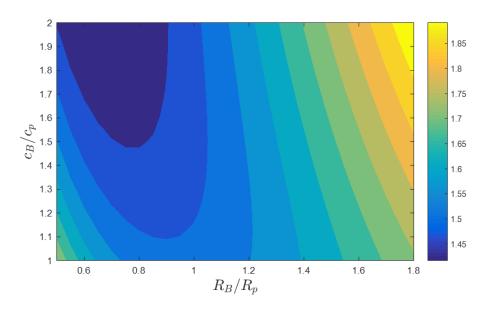
Fig. 4.11. Contours of P_s versus variations of c_B/c_p and R_B/R_p. In these simulations, $l/R_B = 1$, $h/R_B = 0.2$, $\theta_p = \theta_B = 10$ degrees.

as well. It also means, for large values of R_B/R_p , the vehicle has a more tendency to roll than yawing and a significant portion of the propeller's thrust force causes the vehicle to go through a periodic motion in hover, which increases power consumption. Fig 4.12, shows variations of P_s versus variations of R_B/R_p when $c_B/c_p = 2$.
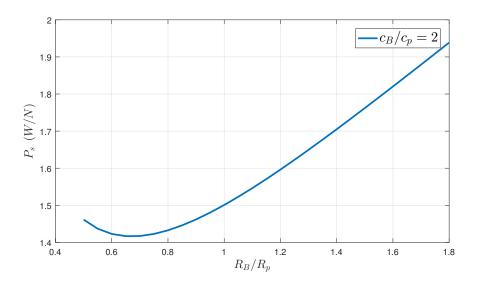
Fig. 4.12. Variations of P_s versus variations of R_B/R_p when $c_B/c_p = 2$.

In addition, the effects of l/R_B ,h/R_B are investigated along with all the other design variables in x. The results show that the power consumption does not vary much with the variations in h/R_B , however, the effects of l/R_B on power consumption can be seen in Fig 4.13. The results indicate that the optimal solution occurs at $l/R_B = 0$, however, the configuration with $l/R_B = 0$ and $\delta = 0$ leads to an uncontrollable configuration (controllability can be checked using (3.42)).

Since the optimal configuration with $l/R_B = 0$ and $\delta = 0$ is uncontrollable, using the additional constraints for trajectory tracking, stated in (4.22), we should
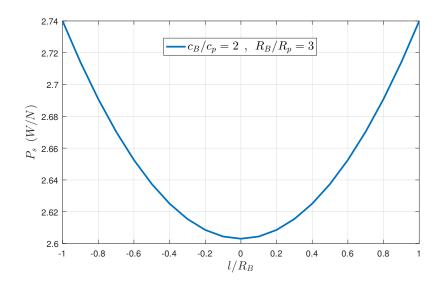
Fig. 4.13. Variations of P_s versus variations of l/R_B.

search for the optimal configuration while minimizing the cost in (4.21). Therefore, in addition to finding the optimal-power configuration in hover, we search for the optimal configuration in terms of trajectory tracking performance. The results show that the optimal solution occurs when $l/R_B = 0.65$ and $R_B/R_p = 0.7$. Note that in (4.22), it is assumed $a_i = 1$ for all $i = 1, 2, , 6$. The variations of the cost function $G(y)$ versus R_B/R_p and l/R_B are presented in Fig 4.14 and Fig 4.15 respectively.

Finally, using (4.21) and by choosing $b_1 = b_2 = 1$, the optimal configuration with the minimum power consumption in hover, $P_s = 1.4168$ W/N, having the best trajectory tracking performance is found as follows:

$$x = \left(\theta_p = 10°, \theta_B = 10°, \frac{c_B}{c_p} = 2, \frac{R_B}{R_p} = 0.7, \frac{l}{R_B} = 0.65, \frac{h}{R_B} = 0, \delta = 0\right) \quad (4.23)$$
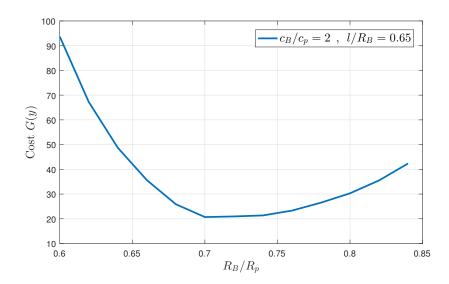
Fig. 4.14. Variations of the cost function $G(y)$ versus R_B/R_p.
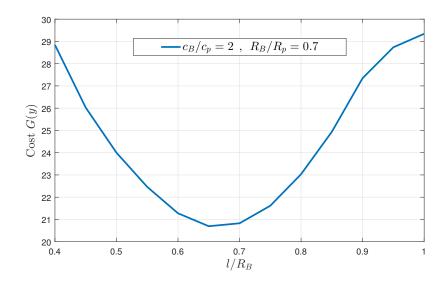
Fig. 4.15. Variations of the cost function $G(y)$ versus l/R_B.

So far, in all the results, it was assumed that the tilting angle is zero. Adding the tilting angle to the equations in monospinner configuration has two consequences:

1. It makes the system of equations highly nonlinear and also in some cases the hover solution does not exist.

2. Due to high nonlinearities and faster rotational motion, a linear time-invariant control strategy may not be able to stabilize and control the reduced attitude of the vehicle and nonlinear control strategies must be employed.
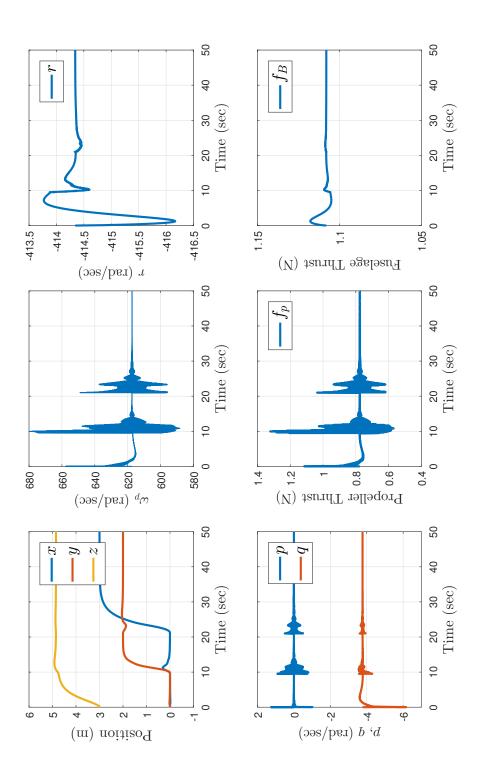
Therefore, finding a feasible hover solution and configuration that is controllable using the proposed control strategy while considering the tilting angle in monospinner may not be easy. However, Monte Carlo simulations of the nonlinear system in different configurations with the proposed control strategy can be carried out to investigate about the probability that the resulting vehicle is able to hover. Needless to say, Monte Carlo simulations for such a system require extensive amount of work and could be a topic for the future works.

In the following, we present the simulation results for the monospinner with the optimal configuration found in (4.23). We assume the total mass of the vehicle is $m = 0.192$ kg where a large portion of it is for battery and electronics which is assumed to be $m_e = 0.120$ kg and the rest of it counts towards propellers and fuselage. Also, with the assumptions given in Section 2, the moment of inertia matrix of the propeller and the fuselage are $\mathbf{I}^p = \mathrm{diag}(7.68 \times 10^{-6}, 7.68 \times 10^{-6}, 1.53 \times 10^{-5})$ kg.m^2

and $\mathbf{I}^B = \text{diag}(4.89 \times 10^{-5}, 4.89 \times 10^{-5}, 1.05 \times 10^{-4})$ kg.m^2 respectively. Using (3.38)-(3.41), the optimal hover solution can be found as follows:

$$\bar{\boldsymbol{n}} = (0, -0.01, 0.999)^T, \ \bar{\boldsymbol{\omega}}_B = (0, -3.77, -414)^T \ \text{rad/s}$$

$$\bar{\boldsymbol{\omega}}_p = 617.37 \ \text{rad/s}, \ \|\bar{\boldsymbol{\tau}}_{d_p}\| = 0.0015 \ \text{N.m}, \ \|\bar{\boldsymbol{\tau}}_{d_B}\| = 0.0031 \ \text{N.m} \tag{4.24}$$

$$\bar{f}_p = 0.39 \ \text{N}, \ \bar{f}_B = 1.10 \ \text{N}, \ \bar{P}_s = 1.41 \ \text{W/N}$$

Using the hover solution, an LQR controller with the weights given in (4.19) is designed to control the reduced attitude of the vehicle. Also, for position control, the natural frequency and damping ratio are all set to 1. The resulting controller is implemented and tested using the nonlinear equations of motion and the physical parameters of the system. Simulation results starting from an initial position $\boldsymbol{d}_0 = (0,0,3)^T$ m to the destination $\boldsymbol{d}_d = (3,2,5)^T$ m (both expressed in the inertial frame) are presented in Fig 4.16.

Note that in these simulations for monospinner, the vehicle starts with initial angular velocity in hover equal to $\bar{\boldsymbol{\omega}}_B$. Because the $\bar{\boldsymbol{\omega}}_B$ is very large (especially the yaw component), the linear time-invariant controller is not able to bring the vehicle from zero angular velocity at takeoff to its equilibrium state in hover, therefore the initial angular velocity in the simulations is set to $\bar{\boldsymbol{\omega}}_B$. This could be a serious problem when implementing the controller on a real system. However, this constraint could also be added to the cost function in (4.21) and also could be accounted for in Monte Carlo simulations in the future works.

Fig. 4.16. Nonlinear simulation results for position control of a monospinner with optimal configuration.

In addition, since the monospinner is highly under-actuated, it can be seen in the top left graph in Fig 4.16, how controlling one degree of freedom could disturb other degrees of freedom. Also it can be seen that there is a steady state error in controlling the z-component of the position (altitude) which may be resolved by adding an integrator to the position controller.

Another important note in these simulations, is the frequency of the response which can be seen in the middle and bottom left graphs of Fig 4.16. In implementing the controller on a real system, it is important to verify that the motors are able to respond to the fast periodic changes in the system.

4.2.2 Bispinners

In this section, optimal solutions for hovering and trajectory tracking of bispinners are presented. Similar to monospinners, we begin with configurations where the tilting angle is zero and continue by investigating the effects of adding tilting angle to the rotors. With that in mind, using (4.16)- (4.21) and using simple blind search algorithm, we investigate about finding the best x which results in the minimum P_s.

Like the monospinner, the results suggest that the optimal-power configuration can be achieved when having the maximum allowed pitch angle for both propeller and fuselage which is 10 degrees. Also, for $\delta = 0$, P_s is independent of l/R_B and h/R_B, therefore, P_s would depend only on two design variables, namely c_B/c_p and R_B/R_p . Fig 4.17 shows the contours of P_s versus c_B/c_p and R_B/R_p . It can be seen that the minimum P_s falls in the dark blue area where $c_B/c_p = 2$, $R_B/R_p = 1.2$ and $P_s =$

0.8852 W/N. Also, Fig 4.18 shows variations of P_s versus R_B/R_p where $c_B/c_p = 2$. Therefore, the optimal configuration with the minimum power consumption in hover is found as follows:

$$x = \left(\theta_p = 10°, \theta_B = 10°, \frac{c_B}{c_p} = 2, \frac{R_B}{R_p} = 1.2, \frac{l}{R_B} = 1, \frac{h}{R_B} = 0, \delta = 0\right) \qquad (4.25)$$
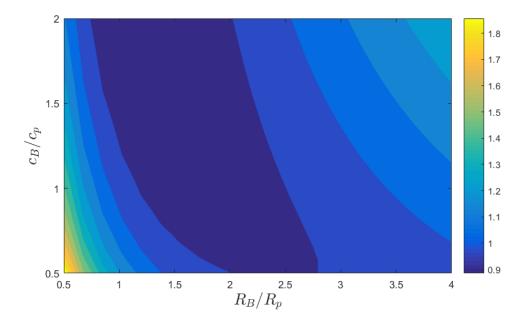
Fig. 4.17. Contours of P_s versus c_B/c_p and R_B/R_p. Note that $l/R_B = 1, h/R_B = 0$ and $\delta = 0$.

Unlike the monospinner, results show that the trajectory tracking performance in bispinner configuration is not much sensitive to the configuration, although in some cases which will be presented later in this section, high nonlinearities due to adding the tilting angle of the rotors might make it difficult to control the vehicle with a
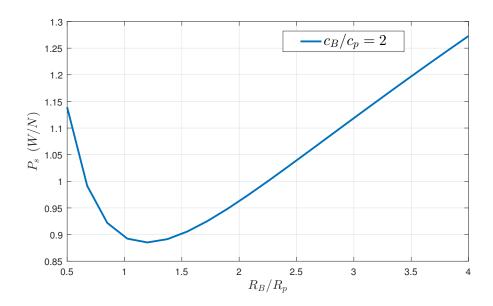
Fig. 4.18. Variations of P_s versus R_B/R_p where $c_B/c_p = 2$. Note that $l/R_B = 1$, $h/R_B = 0$ and $\delta = 0$.

linear time-invariant controller. Therefore, as long as tilting angle δ is zero, (4.25) yields the optimal-power configuration in both hovering and trajectory tracking.

Now, we continue investigating about finding the optimal configuration for the bispinner by considering nonzero tilting angle δ. In this case, the results still suggest the maximum pitch angle for propeller and fuselage's blades. Also, P_s remains insensitive to variations of h/R_B and as shown in Fig 4.17, it is inversely related to c_B/c_p.

Fig 4.19 shows the contours of P_s versus variations of tilting δ and R_B/R_p. It shows that for small values of R_B/R_p the optimal-power hover solution occurs when $\delta = 0$ while, as R_B/R_p increases, the optimal-power hover solution occurs when δ is nonzero and the contours are symmetric with respect to the zero tilting angle.
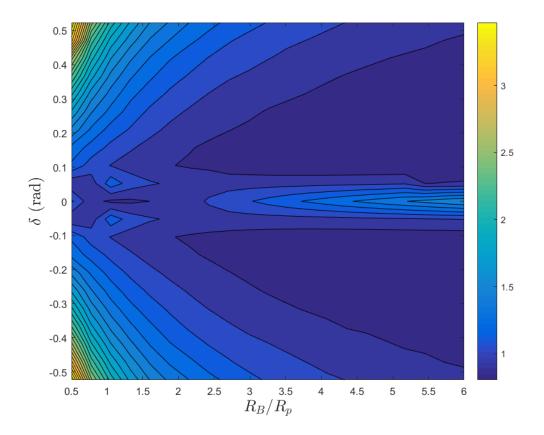
Fig. 4.19. Contours of P_s versus variations of tilting angle δ and R_B/R_p. $c_B/c_p = 2$, $l/R_B = 1$ and $h/R_B = 0$.

Fig 4.20, shows variations of P_s versus variations of tilting angle δ and constant values of R_B/R_p which presents the results of Fig 4.19 clearly. In addition, it shows that as R_B/R_p increases, the minimum-power in each graph decreases which suggests that larger R_B/R_p leads to more optimal configuration.

Fig 4.21 shows three graphs, each presenting variations of the minimum P_s for all values of tilting angle δ versus variations of l/R_B for constant values of R_B/R_p. For example, in the yellow graph where $c_B/c_p = 2$, $l/R_B = 1$, $h/R_B = 0$ and $R_B/R_p = 5.1750$, for each value of l/R_B, the minimum P_s for all values of tilting angle δ is
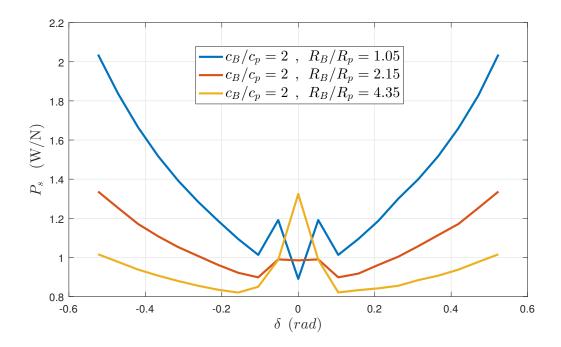
Fig. 4.20. Variations of P_s versus variations of tilting angle δ for constant values of R_B/R_p.

calculated. The results show that as R_B/R_p increases, the minimum P_s occurs at $l/R_B = 1$ while for small values of R_B/R_p, it occurs at $l/R_B < 1$.

According to Fig 4.19 to Fig 4.21, the optimal configuration with the minimum power consumption in hover occurs at a very large R_B/R_p when $l/R_B = 1$. However, such a solution may not be controllable using the proposed linear time-invariant controller. Therefore, to satisfy 4.22, we should constrain the tilting angle to small values $(-0.1 \leq \delta \leq 0.1)$ such that the nominal controller introduced in the previous section can stabilize the vehicle. Therefore, the optimal configuration with the minimum power consumption in hover can be found as shown in Fig 4.22.
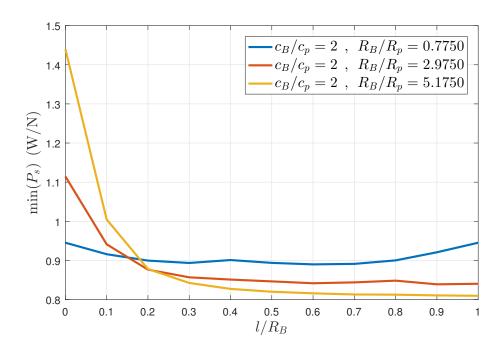
Fig. 4.21. Variations of the minimum P_s for all values of tilting angle δ versus variations of l/R_B for constant values of R_B/R_p.

Note that the trajectory tracking performance in the bispinner is almost insensitive to the configuration as long as the linear time-invariant controller is able to stabilize the vehicle. Finally, the optimal configuration with the minimum power consumption in hover, $P_s = 0.82$ W/N, having the best trajectory tracking performance is the one presented in Fig 4.22 and can be written as follows:

$$x = \left(\theta_p = 10°, \theta_B = 10°, \frac{c_B}{c_p} = 2, \frac{R_B}{R_p} = 5, \frac{l}{R_B} = 1, \frac{h}{R_B} = 0, \delta = 0.1 \right) \qquad (4.26)$$

We continue with presenting simulation results for a bispinner with the optimal configuration found in (37). In this vehicle, $m = 0.384$ kg, $\mathbf{I}^p = \mathrm{diag}(7.68 \times 10^{-6}, 7.68 \times$
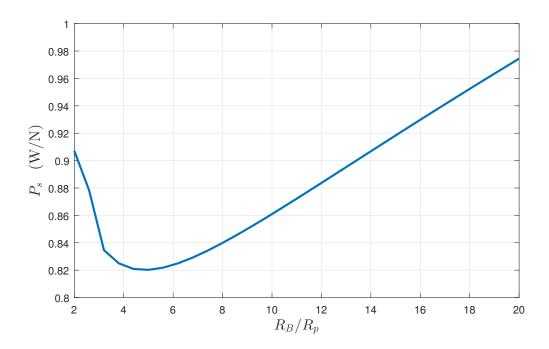
Fig. 4.22. Variations of P_s versus variations of R_B/R_p. The tilting angle is $\delta = 0.1$, $c_B/c_p = 2$, $l/R_B = 1$ and the pitch angle for both propeller and fuselage is 10 degrees.

$10^{-6}, 1.53 \times 10^{-5})$ kg.m^2 and $\mathbf{I}^B = \mathrm{diag}(0.0048, 0.0048, 0.005)$ kg.m^2. The optimal

hover solution can be found as follows:

$$\bar{\boldsymbol{n}} = (0,0,1)^T, \quad \bar{\boldsymbol{\omega}}_B = (0,0,-33.2)^T \text{ rad/s}$$

$$\bar{\omega}_p = 316.93 \text{ rad/s}, \quad \|\bar{\boldsymbol{\tau}}_{d_p}\| = 0.0024 \text{ N.m}, \quad \|\bar{\boldsymbol{\tau}}_{d_B}\| = 0.0520 \text{ N.m} \tag{4.27}$$

$$\bar{f}_p = 0.59 \text{ N}, \quad \bar{f}_B = 2.59 \text{ N}, \quad \bar{P}_s = 0.82 \text{ W/N}$$

Using the above hover solution, an LQR controller with the weights given in (4.19)

is designed to control the reduced attitude of the vehicle. Also, for position control,

the natural frequency and damping ratio are all set to 1. The resulting controller
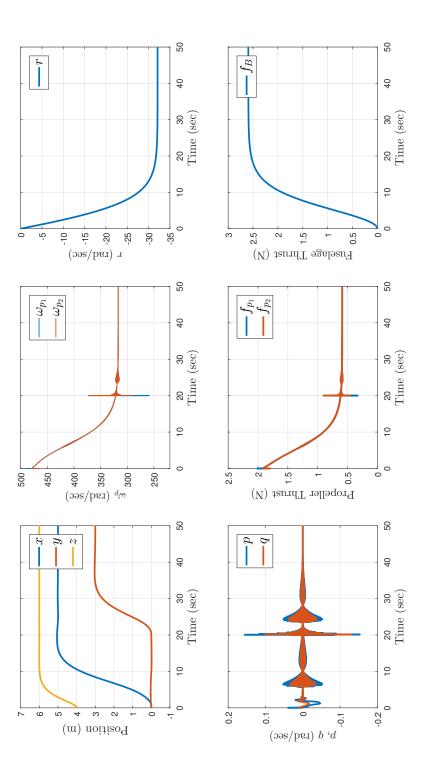
is implemented and tested using the nonlinear equations of motion and the physical parameters of the system. Simulation results starting from an initial position $\boldsymbol{d}_0 = (0, 0, 4)$ m to the destination $\boldsymbol{d}_d = (5, 3, 6)$ m (expressed in the inertial frame) are presented in Fig 4.23.

In the top left graph in Fig 4.23, it can be seen that not only the response of the system is faster, but also it is smoother and almost no overshoot can be seen in the graphs. This is because in bispinner, both roll and pitch moments are balanced, while in monospinner, only roll moments are balanced. According to the top right graph in Fig 4.16, although the vehicle starts with angular velocity zero in its initial position, the linear time-invariant controller is able to bring the vehicle to its equilibrium state.

In the middle and bottom right graphs in Fig 4.23, in the beginning, the yaw rate is zero and the streamline-shape fuselage generates no lift, therefore the propellers must turn at their highest rate in hover to compensate for gravity. However, as the yaw rate increases, the streamline-shape fuselage generates extra lift and therefore propellers must turn slower and generate relatively lower lift to keep the vehicle hovering.

4.2.3   Discussion

This section, in essence, presents a discussion on the results of the performance optimization for spinning UAVs and also a comparison between the two different configurations. We start with the following remarks on the monospinner:

Fig. 4.23. Nonlinear simulation results for position control of a bispinner with optimal configuration.

- It is highly nonlinear and sensitive to geometry and moment of inertia matrix of the fuselage. Therefore, hover solution for an arbitrary geometry may not be feasible.

- For large values of R_B/R_p and l/R_B , the vehicle has more tendency to roll than yaw in which case we may not be able to use linear time-invariant control strategies.

- In hover, only roll moments are balanced and the vehicle has constant pitch and yaw rates. This means that a portion of the thrust will not contribute to compensation of gravity (see Fig. 3), therefore, the COM of the vehicle goes through a periodic motion with nonzero radius in hover which also results in higher power consumption. In addition, controlling one degree of freedom affects other degrees of freedom as well which can be seen in the top left graph in Fig. 16 while controlling the position.

Regarding the bispinner configuration, we summarize the results as follows:

- It is relatively less sensitive to the geometry of the vehicle.

- With roll and pitch moments being completely balanced, as long as there is nonzero yaw rate in the system and for small values of tilting angle δ, linear time-invariant control strategies are applicable.

- For large tilting angles, the deviations from the equilibrium state become so large such that the linear time-invariant model may not be valid anymore and

therefore, the linear time-invariant controller may not be able to stabilize the vehicle.

- Because all forces and moments related to the horizontal motion of the vehicle in the inertial frame are all balanced in hover, the radius of the periodic motion will be zero. In other words, the vehicle will only be spinning about the z-axis of the body frame which is why we always get $\bar{\boldsymbol{n}} = (0, 0, 1)$. This results in having more optimal-power configuration compared to the monospinner.

- Since both roll and pitch moments are balanced and only yaw moment is unbalanced, the control performance is improved compared to the monospinner and it can be seen in the top left graph in Fig. 17 where position control results are shown.

In brief, we can summarize the advantages of bispinner over monospinner as follows:

- Bispinner configuration is more power-optimal

- Control performance is much better in bispinner

- The system is less sensitive to geometry and therefore more design alternatives can be explored

Needless to say, in both configurations, it is important to make sure that the motors can respond properly to the fast periodic changes in the system. For example, in the optimal configuration found for the monospinner in (4.23), the fuselage is

turning at around 400 rad/sec. Thus, the response time of the motors can be added

as a new constraint to the system for the future work.

5

Control for Crash Landing a Quadcopter with a Rotor Failure

As robots have become part of our industries as well as our everyday life, path planning for robots in complex environments has gained significant attention in recent years. Although robots have significant differences in application and their design, path planning and navigation is an essential part in all of them. Given a robot, its dynamics, representation of its environment, its initial state and a goal state, the path planning problem is defined as finding a path from initial state to the goal state which complies with the rules in the environment such as avoiding obstacles. It seems that finding this path is not easy from a computational standpoint. Over the past decades, several different algorithms have been developed some of which are complete, meaning that they return a valid solution in a finite time if one exists and

fail otherwise. Unfortunately, these algorithms usually are not practical due to their complexities [31].

Practical planners using potential fields and cell decomposition methods exist, however they are only practical for state spaces with less than five dimensions [40]-[41]. Recently, sampling-based planning algorithms such as Rapidly-exploring Random Trees (RRT) have proved to be practical and effective in high-dimensional state spaces and have attracted considerable attention in the robotics community. In these algorithms, instead of explicit representation of the environment, by connecting sample points in the obstacle-free space and generating a graph, a feasible path between the initial state and goal state can be found. These algorithms are probabilistically complete [42]. One of the problems with sampling-based algorithms is that they do not necessarily return a global optimal path. However, there is a variant of RRT that is called RRT*, which finds a path that exponentially approaches the global optimal path in the environment as the number of samples approaches infinity [31].

In this section, path planning for emergency landing of a quadcopter is presented. It is assumed that a fairly simple 3D representation of the environment in which the vehicle is flying is available a priori. There are obstacles including all sensitive regions in the environment such as the buildings, trees and lakes which we want to avoid colliding with. Obstacles are assumed to be stationary and cuboid. An example of such representation can be found in Fig 5.1.

For the given map, using Generalized Voronoi Diagram [40] and defining a cost function, the minimum-cost landing spot is found. Using RRT* algorithm an obstacle-
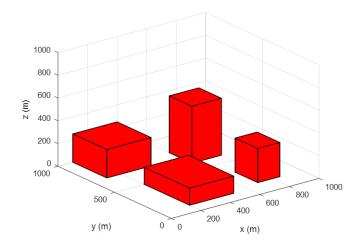
Fig. 5.1. An example map with obstacles. Red cubes represent obstacles.

free path is then found to connect the start point to the landing spot. Finally, using a simple search algorithm the path is shortened further (if possible) and the vehicle performs emergency landing by following it.

5.1 The Best Landing Spot

Selecting the location of landing is an important step in emergency situations, simply because it determines the feasibility of the landing. For example, using the distance of the landing spot from the vehicle and a model to compute total power consumption while following a path, one can determine if the vehicle can safely get to its destination. Also, during the path, the vehicle should maintain a certain distance from the obstacles so that in case of complete power outage it would not collide with any of them. Our goal is to find the best landing spot based on two criteria: (i)

106

finding the safest landing spot with the largest clearance from the obstacles; and (ii) finding an optimal trajectory towards the landing spot.

It is assumed that all obstacles are treated the same, therefore the safest way (in terms of collision) to define clearance is to stay at equal distance from them (if possible). The best way to find such points in a map is to use Generalized Voronoi Diagram (GVD). The algorithm searches all points in the given map and calculates its distance from the closest obstacles and if the distance from at least two obstacles are equal, the point will be added to the GVD [40]. Note that because the z-component of the landing spot is always zero (assuming we always land on the ground), the search only takes place in the x-y plane of the given map. However, in order to make this exhaustive search possible, the map is discretized with a step size which is assumed to be 1 meter in this paper (for larger maps or scaled maps, this step size can be scaled to reduce computation time accordingly). An example of generating GVD for a $1000 \times 1000 \times 1000$ meters map with a step size of 1 meter can be found in Fig 5.2.

To find the best landing spot using GVD, a network of obstacle-free paths (edges of GVD as shown in blue in Fig 5.2) in the x-y plane of the given map is generated. For each point in this network, a cost J as a function of clearance from obstacles and distance from the vehicle is calculated as follows:

$$J(r,d) = a\left(\frac{1}{r}\right) + bd \qquad (5.1)$$
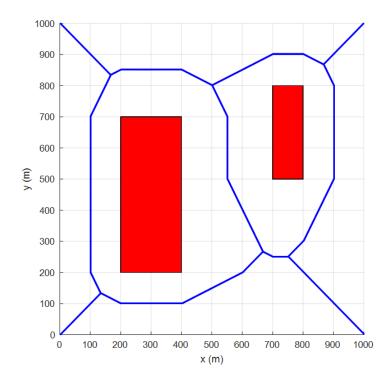
Fig. 5.2. An example of Generalized Voronoi Diagram for a given map of the environment. Blue lines show the GVD.

where a and b are two weights to be determined for the clearance from obstacles represented by r, and distance from the vehicle represented by d, respectively. Finally, by calculating (5.1) for all points in GVD, the point with minimum cost can be selected as the best landing spot. If multiple points are returned, the priority is given to the one with minimum distance from the vehicle.

5.2 Path Planning

In this thesis, RRT* algorithm is used to find the path connecting the position of the vehicle to the landing spot in the given map of the environment. In particular, two different scenarios for path planning are evaluated:

1. When the number of samples are given

2. When the number of samples are unknown

In the first scenario, when the number of samples are given (i.e., 2000 samples), first the graph is generated and then the algorithm attempts to find the shortest path between the start and goal states within that graph (if any exists). Note that in this scenario there is a probability, depending on the number of samples, that the algorithm fails.

The second scenario is slightly different. Instead of using a fixed number of samples, the algorithm keeps adding vertices to the graph until it finds a path between the start and goal states. As the algorithm adds more vertices, the probability of finding a path between the two points approaches 1 and as the number of vertices approaches infinity, the probability of finding the optimal path approaches 1 as well [31].

An additional step is also added to RRT* which minimizes the length of the path further if possible. Due to the random nature of these algorithms, the final path has unnecessary zig-zag like segments which increases the overall length of the path. To avoid these, a search over the vertices on the final path is performed to find the shortest path among its vertices connecting the start state to the goal state.

In summary, the path planning problem for emergency landing of a quadcopter experiencing one rotor failure can be done using one of the proposed scenarios to connect the initial position of the vehicle to the best landing spot found by the proposed algorithm in the previous section.

5.3 Crash Landing

This section presents simulation results for emergency landing of a quadcopter with one rotor failure. A vehicle with the same specifications introduced in Section 3.1 and with the hover solution given in (4.15) is used in the simulations. All steps can be summarized as follows:
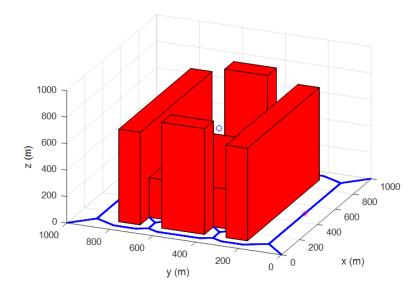
1. Finding the optimal hover solution after failure

2. Design of the fault tolerant controller

3. Finding the best landing spot

4. Finding the path between position of the vehicle and the landing spot

5. Following the path and landing the vehicle.

Suppose for the quadcopter after failure, an LQR controller, with the weight matrix for reduced attitude states being $\mathbf{Q} = \text{diag}([1, 1, 20, 20])$ and $\mathbf{R} = 1$ being the weight matrix for the control inputs, is designed for the optimal hover solution as found in (4.15). For position control, damping ratio $\xi = 0.65$ and natural frequency $\omega_n = 0.8$ are selected for all x, y and z coordinates. Representation of the environment
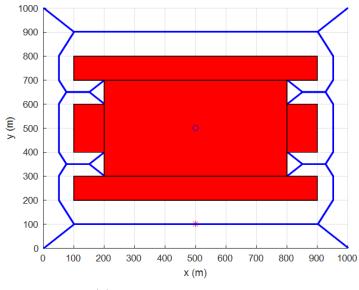
is shown in Fig 5.3, with obstacles being red. Assume the initial position of the vehicle after failure is at $\boldsymbol{d}_0 = (500, 500, 550)^T$ expressed in the inertial frame and as represented by a small blue circle in the map. By generating GVD for the given map as shown in blue in Fig. 11, and using the cost function defined in (5.1) with $a = 100$ and $b = 1$ the best landing spot is found to be at $\boldsymbol{d}_d = (500, 101, 0)^T$ as represented by a magenta asterisk. Note that in finding the best landing spot, $a \gg b$ gives the priority to the clearance from obstacles in the map.

Based on the second scenario for path planning and by setting the step size for RRT* algorithm to 50 meters and the radius of the circle to rewire the graph to 150 meters, a path is found between the start and goal states which is shown in magenta in Fig 5.4 and by searching through the vertices of this path the shortest path can be retrieved as shown in yellow. Finally, by implementing the controller for the nonlinear simulation of the quadcopter flight, the vehicle follows the yellow path and lands the vehicle safely. The actual path of the quadcopter following the yellow path is represented by dashed black line in Fig 5.4.

It can be seen that the controller can successfully track the path with small deviations and lands the vehicle safely.

(a) Representation in 3D space

(b) Representation in x-y plane

Fig. 5.3. Representation of the environment. Obstacles are shown in red, GVD is represented by blue lines, initial position of the vehicle is represented by blue circle and the best landing spot is represented by magenta asterisk.

(a) Representation in 3D space

(b) Representation in x-y plane
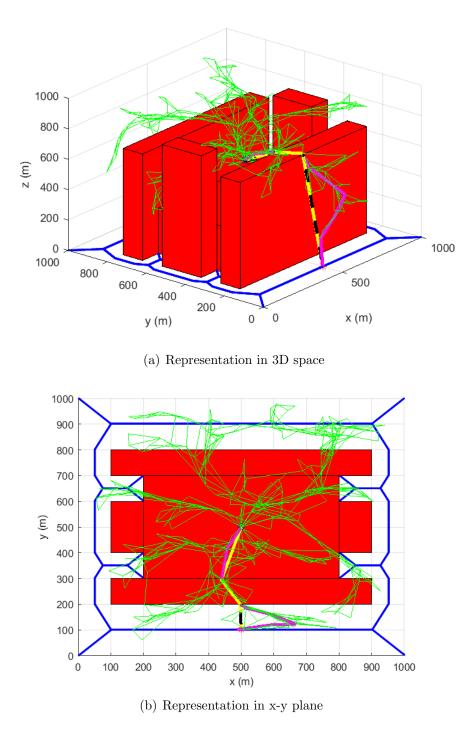
Fig. 5.4. Path planning and path following simulation results. RRT*
graph is represented by green, the initial path found by the algorithm
is shown in magenta, the final shortest path is shown in yellow and
the actual path of the quadcopter is shown in dashed black line.

113

6

Conclusions and Future Works

In this thesis, modeling and control of multi-rotor UAVs with focus on their safety and performance are presented. We devoted a chapter to mathematical modeling of multi-rotor UAVs. For the first time, we included a complete mathematical model of propellers, in presence of uniform freestream, in modeling multi-rotor UAVs. In particular, two specific types of multi-rotor UAVs are studied in this thesis: i) quadcopters with angled thrust vecotrs; and ii) spinning UAVs with streamline-shape fuselage. For the spinning UAVs, we studied two different configurations namely *monospinner* and *bispinner*.

In Chapter 3, first, control design for a quadcopter with angled thrust vectors is presented along with nonlinear simulation results demonstrating position control of the vehicle. Second, fault-tolerant control design in quadcopters with one rotor failure is studied where a new hover definition after failure is presented. Based on

the new definition of hover, a new equilibrium is found for the system and a linear time-invariant system is introduced describing behavior of the system close to the equilibrium state. Then, a linear time-invariant control strategy (e.g, LQR) is developed for the linear model to control the attitude and position of the vehicle after failure. Third, a control strategy to control attitude and position of a spinning UAV with streamline-shape fuselage, in both configurations, is presented for the first time along with nonlinear simulations validating the results. In addition, controllability of spinning UAVs is investigated in this chapter.

In Chapter 4, the performance of multi-rotor UAVs is investigated. In Section 4.1.1, we present the effects of angled thrust vectors and the position of COM of the vehicle with respect to the propellers' plane on stability and maneuverability of quadcopters. The effects of tilting angles (dihedral and twist angles) on the thrust generated by propellers and consequently on stability of the system were introduced afterwards. Transfer functions considering pure yaw motion were derived followed by stability analysis and formulation of a yaw damper produced by adding twist angles to the rotors for a specific configuration. Six different configurations based on these angles were introduced and were ranked based on stability and maneuverability. One of those configurations led to finding the most stable design with intrinsic damping in roll, pitch and yaw motion. The formulation for these dampers was presented followed by stability analysis in yaw motion. The dampers in the system would be favorable for applications where the vehicle hovers such as imaging, surveillance and monitoring. They will be unfavorable when the vehicle is in motion and maneuverability is needed.

As a future work, a reconfigurable system can be designed in a way to transform from the most stable system to the most maneuverable system in the respective situation and vice versa. Such vehicle will be able to change dihedral and twist angles on the fly in order to transform to the required configuration. Another possible future work is to find the optimized values for dihedral and twist angles. Two different optimization problems can be defined: 1) optimizing the angles for the most stable configuration; and 2) optimizing the angles for the most maneuverable configuration. Finally, verifying the results of this paper using experiments will be done in a future work as well. In addition, in the design of monospinner, a specific configuration inspired from nature can be analyzed where the geometry of the fuselage is designed similar to that of a maple seed. This configuration might lead to the design of fault tolerant controllers in monospinners in case of rotor failure as if the only rotor failed, the vehicle will slowly descend and land without major physical damage to its fuselage. This could be another topic for the future works.

In Section 4.1.2, using the results of Section 4.1.1 and the control strategy developed for a quadcopter experiencing a rotor failure, a specific configuration for quadcopters is introduced which not only results in better stability in yaw motion but also yields the minimum-power hover solution in case of a rotor failure. In this configuration, if a rotor fails, the other rotor turning in the same direction as the failed motor must be shut down and then the controller stabilizes the vehicle with the two remaining functioning rotors. This is due to adding twist angles to the rotors.

If the twist angle is zero, all the three remaining functioning motors will be turning and the power consumption will not be the minimum.

In section 4.2, a set of design variables are defined and an optimization problem in introduced to find the optimal configurations for both monospinner and bispinner which not only are power optimal in hover, but also optimal for tracking a trajectory. By solving the optimization problem, the optimal configurations are found. In addition, the effects of all the design variables on power consumption of the vehicle are investigated separately and results are presented. In the end, nonlinear simulation results for position control and a comparison between the two configurations along with design guidelines are presented. The results suggest that the bispinner has several advantages over the monospinner configurations including but not limited to: i) lower power consumption; ii) better trajectory tracking performance; and iii) less sensitive to geometry of the fuselage. For the future work, one interesting topic may be investigating about finding the best geometry in monospinner configuration which is controllable using the proposed linear time-invariant controller which can be done using Monte Carlo simulations, through which, sensitivity analysis can be done as well. Developing a nonlinear control strategy for controlling the reduced attitude of the vehicle could also be a topic for the future works. Another topic for the future work is of course experimenting the vehicle with optimal configurations and compare the results with that of simulations.

Finally, Chapter 5 presents a framework for emergency landing of quadcopters in case of complete failure of a rotor. We consider emergency landing of a quadcopter

with angled thrust vectors experiencing a rotor failure with the optimal configuration presented in Section 4.1.2. Also, for the configuration with minimum power consumption, cascaded control strategy is used to control attitude and position of the vehicle. For landing, first, an algorithm is proposed to find the best landing spot in a given map of the environment where obstacles are represented by cuboids. Two parameters are used to define a cost function in order to find the optimal landing spot in the given map: (i) finding the safest landing spot with the largest clearance from the obstacles; and (ii) finding an optimal trajectory towards the landing spot. In order to properly define the clearance from obstacles, Generalized Voronoi Diagram (GVD) is used. For all points on the GVD, the one with minimum cost is selected as the best landing spot. A finite horizon is selected in generating the GVD. The boundary of this horizon is estimated based on the total cost-to-go based on the power requirement. Furthermore, due to the size and dimensionality of the search space, an RRT*-type randomized motion planning strategy is used which can generate sub-optimal trajectories on the fly in real time. Using nonlinear simulations and the designed controller, the results of following the generated path (from RRT*) and performing emergency landing are evaluated. The results show that the quadcopter perfectly tracks the trajectory and lands the vehicle safely. Finally, verifying the results by experiments and performing sensitivity analysis can be topics for the future work.

REFERENCES

REFERENCES

[1] J. Thomas, J. Polin, K. Sreenath, , and V. Kumar, "Avian-inspired grasping for quadcopter micro uavs," *Bioinspiration & Biomimetics*, vol. 9, pp. 25 010–25 019, 2014.

[2] J. Rasmussen, J. Nielsen, F. Garcia-Ruiz, S. Christensen, and J. C. Streibig, "Potential uses of small unmanned aircraft systems (uas) in weed research," *Weed Research*, vol. 4, no. 53, pp. 242–248, 2013.

[3] J. R. Horandel, S. Buitink, A. Corstanje, J. E. Enriquez, , and H. Falcke, "The lofar radio telescope as a cosmic ray detector," in *International Cosmic Ray Conference*, 2013.

[4] M. Muller, S. Lupashin, and R. D'Andrea, "Tquadrocopter ball juggling," in *2017 IEEE/RSJ International Conference on Intelligent Robots and Systems (IROS)*, 2011, pp. 5113–5120.

[5] L. F. Luque-Vega, B. Castillo-Toledo, A. Loukianov, and L. E. Gonzalez-Jimenez, "Power line inspection via an unmanned aerial system based on the quadrotor helicopter," in *MELECON 2014 - 17th IEEE Mediterranean Electrotechnical Conference*, April 2014, pp. 393–397.

[6] S. Bouabdallah and R. Siegwart, "Full control of a quadcopter," in *2007 IEEE/RSJ International Conference on Intelligent Robots and Systems*, 2007, pp. 153–158.

[7] M. D. Hua, T. Hamel, P. Morin, and C. Samson, "A control approach for thrust-propelled underactuated vehicles and its application to vtol drones," *IEEE Transactions on Automatic Control*, vol. 54, no. 8, pp. 1837–1853, Aug 2009.

[8] R. Mahony, V. Kumar, and P. Corke, "Multirotor aerial vehicles: Modeling, estimation, and control of quadrotor," *IEEE Robotics Automation Magazine*, vol. 19, no. 3, pp. 20–32, Sept 2012.

[9] M. Y. Amir and V. Abbass, "Modeling of quadrotor helicopter dynamics," in *International Conference on Smart Manufacturing Application*, 2008, pp. 100–105.

[10] D. Mellinger, N. Michael, and V. Kumar, "Trajectory generation and control for precise aggressive maneuvers with quadrotors," *The International Journal of Robotics Research*, vol. 31, no. 5, pp. 664–674, 2012.

[11] J. Wang, T. Bierling, M. Achtelik, L. Hocht, F. Holzapfel, W. Zhao, and G. Hiong, "Attitude free position control of a quadcopter using dynamic inversion," in *AIAA Infotech@ Aerospace*, 2011, pp. 29–31.

[12] M. Hedayatpour, M. Mehrandezh, and F. Janabi-Sharifi, "A unified approach to configuration-based dynamic analysis of quadcopters for optimal stability," in *2017 IEEE/RSJ International Conference on Intelligent Robots and Systems (IROS)*, Sept 2017, pp. 5116–5121.

[13] M. Hedayatpour, M. Mehrandezh, and F. Janabi-Sharifi, "Revised propeller dynamics and energy-optimal hovering in a monospinner," in *The 4th International Conference of Control, Dynamic Systems, and Robotics*, August 2017, pp. 1–8.

[14] W. Zhang, M. W. Mueller, and R. D'Andrea, "A controllable flying vehicle with a single moving part," in *2016 IEEE International Conference on Robotics and Automation (ICRA)*, May 2016, pp. 3275–3281.

[15] J. Paulos and M. Yim, "An underactuated propeller for attitude control in micro air vehicles," in *2013 IEEE/RSJ International Conference on Intelligent Robots and Systems (IROS)*, 2016, pp. 1374–1379.

[16] E. R. Ulrich, D. J. Pines, , and J. S. Humbert, "From falling to flying: the path to powered flight of a robotic samara nano air vehicle," *Bioinspiration & Biomimetics*, vol. 5, no. 4, pp. 45 009–45 025, 2010.

[17] K. Y. Ma, P. Chirarattananon, S. B. Fuller, , and R. J. Wood, "Controlled flight of a biologically inspired, insect-scale robot," *Science*, vol. 340, no. 6132, p. 603607, 2013.

[18] M. W. Mueller and R. D'Andrea, "Relaxed hover solutions for multicopters: application to algorithmic redundancy and novel vehicles," *International Journal of Robotics Research*, vol. 35, no. 8, pp. 873–889, 2015.

[19] http://www.modlabupenn.org/2016/10/27/piccolissimo, 2016.

[20] M. Dammar, "Reduced visibility rotorcraft and method of controlling flight of reduced visibility rotorcraft," Patent US 20 060 214 051, 09 28, 2006. [Online]. Available: https://www.google.com/patents/US20060214051

[21] J. E. Low, L. T. S. Win, D. S. B. Shaiful, C. H. Tan, G. S. Soh, and S. Foong, "Design and dynamic analysis of a transformable hovering rotorcraft (thor)," in *2017 IEEE International Conference on Robotics and Automation (ICRA)*, 2017, pp. 6389–6396.

[22] A. reddi, A. Lanzon, and S. Longhi, "A feedback linearization approach to fault tolerance in quadrotor vehicles," in *Proceedings of the 18th IFAC world congress*, September 2011, pp. 5413–5418.

[23] M. W. Mueller and R. D'Andrea, "Stability and control of a quadrocopter despite the complete loss of one, two, or three propellers," in *2014 IEEE International Conference on Robotics and Automation (ICRA)*, 2014, p. 4552.

[24] M. Ryll, H. H. Bulthoff, and P. R. Giordano, "Modeling and control of a quadcopter uav with tilting propellers," in *2012 IEEE International Conference on Robotics and Automation (ICRA)*, 2012, pp. 4606–4613.

[25] D. Scaramuzza, M. Achtelik, L. Doitsidis, and et al, "Vision-controlled micro flying robots: from system design to autonomous navigation and mapping in gps-denied environments," *IEEE Robotics Automation Magazine*, vol. 21, no. 3, pp. 26–40, 2014.

[26] A. Marks, J. F. Whidborne, and I. Yamamoto, "Control allocation for fault tolerant control of a vtol octorotor," in *UKACC international conference on control*, September 2012, pp. 357–362.

[27] V. Lippiello, F. Ruggiero, and D. Serra, "Emergency landing for a quadrotor in case of a propeller failure: A backstepping approach," 2014 IEEE/RSJ International Conference on Intelligent Robots and Systems (IROS), p. 47824788.

[28] D. Mellinger, N. Michael, and V. Kumar, "Trajectory generation and control for precise aggressive maneuvers with quadcopters," *Experimental Robotics*, vol. 3, p. 361373, 2014.

[29] M. Hehn and R. D'Andrea, "Quadrocopter trajectory generation and control," in *18th IFAC World Congress, Milano*, 2011, pp. 1485–1491.

[30] S. M. LaValle, "Rapidly-exploring random trees: A new tool for path planning," http://janowiec.cs.iastate.edu/papers/rrt.ps, 8 1998, tR 98-11, Computer Science Dept., Iowa State Univ.

[31] S. Karaman and E. Frazzoli, "Sampling-based algorithms for optimal motion planning," *International Journal of Robotics Research*, vol. 30, no. 7, pp. 846–894, 2011.

[32] M. Cutler and J. How, "Actuator constrained trajectory generation and control for variable-pitch quadcopters," in *Proc. AIAA Guidance, Navigation, and Control Conference*, Minneapolis, MN, USA, 2012, pp. 1–15.

[33] D. Brescianini and R. DAndrea, "Design, modeling and control of an omni-directional aerial vehicle," in *2016 IEEE International Conference on Robotics and Automation (ICRA)*, Stockholm, Sweden, 2016, pp. 3261–3266.

[34] D. Falanga, E. Mueggler, M. Faessler, and D. Scaramuzza, "Aggressive quadrotor flight through narrow gaps with onboard sensing and computing using active vision," in *2017 IEEE International Conference on Robotics and Automation (ICRA)*, Singapore, 2017, pp. 5774–5781.

[35] S. Rajappa, M. Ryll, H. H. Blthoff, and A. Franchi, "Modeling, control and design optimization for a fully-actuated hexarotor aerial vehicle with tilted propellers," in *2015 IEEE International Conference on Robotics and Automation (ICRA)*, Seattle, WA, USA, 2015, pp. 4006–4013.

[36] "Cyphy works," https://www.cyphyworks.com/products/parc, 2015.

[37] J. D. Anderson, *Fundamentals of Aerodynamics*, 5th ed. United States: McGraw Hill Higher Education, 2016.

[38] "Experimental data for naca airfoils," http://m-selig.ae.illinois.edu/ads/coord_database.html.

[39] P. H. Zipfel, *Modeling and Simulation of Aerospace Vehicle Dynamics*, 2nd ed. United States: AIAA Education Series, 2007.

[40] P. Corke, *Robotics, Vision and Control*, 1st ed. Springer-Verlag Berlin Heidelberg, 2011.

[41] O. Khatib, "Real-time obstacle avoidance for manipulators and mobile robots," *The International Journal of Robotics Research*, vol. 5, no. 1, pp. 90–98, 1986.

[42] T. Lozano-Perez and M. A. Wesley, "An algorithm for planning collision-free paths among polyhedral obstacles," *Communications of the ACM*, vol. 22, no. 10, pp. 560–570, 1979.

APPENDIX

A

Rotation Matrices

Transformation from body frame B to inertial frame I can be found using a combination of three different rotations. In this thesis, we follow the conventional rotation sequence, roll-pitch-yaw, used in aerospace applications as follows:

$$^{I}\mathbf{R}_B = \mathbf{R}_z(\psi)\mathbf{R}_y(\theta)\mathbf{R}_x(\phi) \tag{A.1}$$

By expanding the rotation matrices, we get:

$$\mathbf{R}_x(\phi) = \begin{bmatrix} 1 & 0 & 0 \\ 0 & \cos\phi & \sin\phi \\ 0 & -\sin\phi & \cos\phi \end{bmatrix} \tag{A.2}$$

$$\mathbf{R}_y(\theta) = \begin{bmatrix} \cos\theta & 0 & -\sin\theta \\ 0 & 1 & 0 \\ \sin\theta & 0 & \cos\theta \end{bmatrix} \tag{A.3}$$

$$\mathbf{R}_z(\psi) = \begin{bmatrix} \cos\psi & \sin\psi & 0 \\ -\sin\psi & \cos\psi & 0 \\ 0 & 0 & 1 \end{bmatrix} \tag{A.4}$$

Finally, we can rewrite and simplify (A.1) as follows:

$$^{I}\mathbf{R}_B = \begin{bmatrix} c_\theta c_\psi & s_\phi s_\theta c_\psi - c_\phi s_\psi & s_\phi s_\psi + c_\phi s_\theta c_\psi \\ c_\theta s_\psi & c_\phi c_\psi + s_\phi s_\theta s_\psi & c_\phi s_\theta s_\psi - s_\phi c_\psi \\ -s_\theta & s_\phi c_\theta & c_\phi c_\theta \end{bmatrix} \tag{A.5}$$

where s and c represent sin and cos functions respectively. Note that the same rotation sequence is used for transforming from motor frame M_i to body frame B.

VITA

Mojtaba Hedayatpour

Born June 20, 1992

Master of Applied Science, Industrial Systems Engineering	2015-2018

Supervisor: Prof. Mehran Mehrandezh from University of Regina

Co-supervisor: Prof. Farrokh Janabi-Sharifi from Ryerson University

University of Regina, Canada

Bachelor of Science, Aerospace Engineering	2010-2014

Sharif University of Technology, Tehran, Iran

Publications

- **Mojtaba Hedayatpour**, Mehran Mehrandezh, Farrokh Janabi-Sharifi, *"Propeller Performance in Presence of Freestream"*, to appear in *"Proceedings of The Canadian Society for Mechanical Engineering International Congress 2018"* (***CSME'18***), May 27-30, **2018**, Toronto, On, Canada.

- **Mojtaba Hedayatpour**, Mehran Mehrandezh, Farrokh Janabi-Sharifi, *"Modeling, Control and Simulation of a Holonomic and Power Efficient Multi-rotor UAV"*, to appear in 2018 *"**AIAA** Atmospheric Flight Mechanics Conference"*, June 25-29, **2018**, Atlanta, Georgia, USA.

- **Mojtaba Hedayatpour**, Mehran Mehrandezh, Farrokh Janabi-Sharifi, *"Optimal-power Configurations for Hover Solutions in Mono-spinners"*, arXiv preprint arXiv:1709.07969v1, September **2017**.

- **Mojtaba Hedayatpour**, Mehran Mehrandezh, Farrokh Janabi-Sharifi, *"A Unified Approach in Configuration-based Dynamic Analysis of Quadcopters for Optimal Stability"*, in 2017 *"IEEE/RSJ International Conference on Intelligent Robots and Systems (**IROS'17**)"*, September **2017**, Vancouver, Canada.

- **Mojtaba Hedayatpour**, Mehran Mehrandezh, Farrokh Janabi-Sharifi, *"Design and Development of a Holonomic and Power Efficient Multi-rotor UAV"*, in 2017 *"IEEE/RSJ International Conference on Intelligent Robots and Systems (**IROS'17**)"*, September 24-28, **2017**, Vancouver, Canada. [**Poster**]

- **Mojtaba Hedayatpour**, Mehran Mehrandezh, Farrokh Janabi-Sharifi, *"Revised propeller dynamics and energy-optimal hovering in a monospinner'*, in the *"Proceedings of the 4th International Conference of Control, Dynamic Systems, and Robotics (**CDSR'17**)"*, August **2017**, Toronto, Canada, pp. 135-1 - 135-8. [**Best Paper Award**]